

Conjugate heat and mass transfer in the lattice Boltzmann equation methodLike Li,^{*} Chen Chen,[†] Renwei Mei,[‡] and James F. Klausner[§]*Department of Mechanical and Aerospace Engineering, University of Florida, Gainesville, Florida 32611-6250, USA*

(Received 6 December 2013; revised manuscript received 7 March 2014; published 22 April 2014)

An interface treatment for conjugate heat and mass transfer in the lattice Boltzmann equation method is proposed based on our previously proposed second-order accurate Dirichlet and Neumann boundary schemes. The continuity of temperature (concentration) and its flux at the interface for heat (mass) transfer is intrinsically satisfied without iterative computations, and the interfacial temperature (concentration) and their fluxes are conveniently obtained from the microscopic distribution functions without finite-difference calculations. The present treatment takes into account the local geometry of the interface so that it can be directly applied to curved interface problems such as conjugate heat and mass transfer in porous media. For straight interfaces or curved interfaces with no tangential gradient, the coupling between the interfacial fluxes along the discrete lattice velocity directions is eliminated and thus the proposed interface schemes can be greatly simplified. Several numerical tests are conducted to verify the applicability and accuracy of the proposed conjugate interface treatment, including (i) steady convection-diffusion in a channel containing two different fluids, (ii) unsteady convection-diffusion in the channel, (iii) steady heat conduction inside a circular domain with two different solid materials, and (iv) unsteady mass transfer from a spherical droplet in an extensional creeping flow. The accuracy and order of convergence of the simulated interior temperature (concentration) field, the interfacial temperature (concentration), and heat (mass) flux are examined in detail and compared with those obtained from the “half-lattice division” treatment in the literature. The present analysis and numerical results show that the half-lattice division scheme is second-order accurate only when the interface is fixed at the center of the lattice links, while the present treatment preserves second-order accuracy for arbitrary link fractions. For curved interfaces, the present treatment yields second-order accurate interior and interfacial temperatures (concentrations) and first-order accurate interfacial heat (mass) flux. An increase of order of convergence by one degree is obtained for each of these three quantities compared with the half-lattice division scheme. The surface-averaged Sherwood numbers computed in test (iv) agree well with published results.

DOI: [10.1103/PhysRevE.89.043308](https://doi.org/10.1103/PhysRevE.89.043308)

PACS number(s): 47.11.-j, 44.35.+c, 44.05.+e, 47.55.N-

I. INTRODUCTION

Conjugate heat (mass) transfer with the continuity of temperature (concentration) and heat (mass) flux at the fluid-solid interface or at the interface of two solids or fluids of different thermal (mass diffusion) properties have been extensively studied for their scientific and engineering significance [1–8]. The problems of conjugate heat (mass) transport across an interface occur in a wide range of applications, such as cooling of turbine blades, heat exchangers and electronic devices, thermal insulation on heat pipes and chemical reactors, heat conduction in composite materials, and heat and mass transfer between solid particles and their surrounding fluids. Efficient and accurate implementation of conjugate heat and mass transfer conditions is also of great importance in the study of transport phenomena on micro-/mesoscopic levels, such as pore-scale determination of effective thermal conductivity and diffusivity of porous structures and chemical reactions in microchannels and microreactors [9–12].

When using conventional computational fluid dynamics (CFD) methods such as finite-difference, finite-volume, and finite-element methods for conjugate heat and mass transfer [1–8], a popular approach to implement the conjugate

interface condition is to apply iterative schemes, in which a Dirichlet interface condition is imposed for one phase and a Neumann interface condition for the other (two solids or fluids of different thermal or mass diffusion properties are also considered as two phases in this study). The heat and mass transfer in each phase is separately solved and the continuity condition at the interface is satisfied after multiple iterations. In these iterative schemes, extrapolation is usually required to obtain the temperature (concentration) and their fluxes at the interface. For conjugate transport problems with complex interface geometry, the iterative schemes may become difficult to implement and they normally necessitate a considerable amount of computational effort.

The lattice Boltzmann equation (LBE) method has become an attractive alternative numerical method for the convection-diffusion equation (CDE) for heat and mass transfer [see Refs. [13–15] and references therein]. The most well-known features of the LBE method include its inherent explicit algorithm and the capability to treat complex geometry. Boundary condition treatment is essential to the integrity of the LBE method for heat and mass transfer since the kinetics-based LBE method deals directly with the microscopic distribution functions rather than the macroscopic temperature or concentration. Based on their second-order accurate boundary treatments proposed for both the Dirichlet and Neumann conditions, Li *et al.* [14,15] have established a general framework for heat and mass transfer simulations using the LBE method with direct extension to curved boundary situations. In their framework, explicit analytical expressions

^{*}Corresponding author: likelichina@ufl.edu[†]alex8937@ufl.edu[‡]rwmei@ufl.edu[§]klaus@ufl.edu

were developed to relate the macroscopic quantities, such as boundary temperature (concentration) and their fluxes and interior temperature (concentration) gradients, to the microscopic distribution functions solved in the LBE model. To enrich that framework and make the LBE method an effective numerical method for conjugate heat and mass transport modeling, an accurate and efficient interface treatment is desired.

An interface, when assumed to have zero thickness, is essentially a common boundary for the two adjacent phases or subdomains. While different from the standard Dirichlet and Neumann boundary conditions where the respective boundary temperature (concentration) and boundary flux are explicitly prescribed, the boundary conditions at an interface are conjugate ones pertaining to the continuity of the unknown interfacial variable and its flux. The first work that explicitly addressed the fluid-solid interface condition in the LBE method was conducted by Wang *et al.* [9]. They proposed a simple “half-lattice division” treatment for conjugate heat transfer simulations. No special treatment is required in their interface scheme and the continuity condition at the interface can be automatically satisfied for steady cases. Their scheme was numerically verified with steady-state tests when the straight interfaces were fixed at the center of the lattice links. This half-lattice division treatment was applied in [10,11] to predict the effective thermal conductivity of various porous structures. It was also employed by Tarokh *et al.* [16] to simulate the conjugate heat transfer between two fluid streams at different temperatures and separated by a solid layer of finite thickness. Meng *et al.* [17] theoretically analyzed the continuity of temperature and heat flux at a fluid-solid interface in the LBE method. They derived a closed system of equations for the unknown distribution functions at the interface for both the fluid and the solid domains. It is noticed that, different from the half-lattice division treatment in [9], the interface scheme in [17] requires that the interface be located exactly on the lattice nodes. This “lattice node on the interface” scheme was also applied by Imani *et al.* [18] to simulate the conjugate heat transfer from heated obstacles mounted in a channel. Seddiq *et al.* [19] also modeled conjugate heat transfer with the LBE method by fixing the interface on a row of lattice nodes and further assuming that the ratio of the gradients of the microscopic distribution functions for the two phases at the interface is inversely proportional to their thermal conductivity ratio. The applicability of their interface scheme was demonstrated with two numerical tests, although they did not provide any theoretical proof for their assumption of proportionality on the microscopic distribution function level; in addition, the continuity of temperature and heat flux at the interface was not verified in [19].

It is realized that the existing interface schemes in the LBE method for conjugate heat and mass transfer are limited to straight-interface geometry, and the location of any interface node in the lattice is fixed either halfway between two lattice nodes [9,19] or right at a lattice node [17,18]. Thus, those interface schemes are not directly applicable to conjugate transport problems involving curved interface geometry, where the lattice links are intersected by the curved interface with irregular link fractions. In addition, the order of accuracy of the conjugate interface schemes has not been investigated in

previous studies. It is the objective of the present study to develop a general interface treatment that is applicable to curved interfaces in conjugate heat and mass transfer modeling with the LBE method. The exactness of the local interface geometry is preserved in the present treatment based on our previously proposed Dirichlet and Neumann boundary condition treatments in the LBE method [14]. The schemes used to evaluate the interfacial temperature (concentration) and interfacial fluxes are also presented. The accuracy of the present interface treatment is systematically investigated. The investigation includes the convergence orders of the interior temperature (concentration) fields and the interfacial values and their fluxes.

The rest of this paper is organized as follows. In Sec. II, the multiple-relaxation-time (MRT) LBE model for the general CDE is introduced. Section III summarizes our previous Dirichlet and Neumann boundary treatments, which serve as the basis for the present interface treatment development. The general interface treatment for conjugate heat and mass transfer is derived in Sec. IV, in which a decoupled treatment for special cases such as straight interfaces and zero-tangential-gradient curved interfaces is also provided. Four numerical tests are presented in Sec. V to verify the applicability and accuracy of the present interface schemes. Section VI concludes the paper.

II. LATTICE BOLTZMANN MODEL FOR THE CONVECTION-DIFFUSION EQUATION

The governing equation for heat and mass transport can be considered as a general CDE

$$\frac{\partial \phi}{\partial t} + \frac{\partial}{\partial x_j} (v_j \phi) = \frac{\partial}{\partial x_i} \left(D_{ij} \frac{\partial \phi}{\partial x_j} \right) + G, \quad (1)$$

where the scalar variable ϕ can be either temperature or concentration in heat or mass transfer problems, respectively, t is the time, v_j is the velocity component in the x_j direction, D_{ij} is the diffusion coefficient, and G is the general source term.

There have been various LBE models proposed (see Refs. [13–15] and references therein) for the CDE (1). The MRT D3Q7 and D2Q5 ($DnQm$ denotes m discrete lattice velocities in n dimensions) models proposed by Yoshida and Nagaoka [13] are used in the present work for their simple implementation, second-order accuracy in space and first-order accuracy in time, and the capability to simulate anisotropic diffusion problems.

To recover the macroscopic CDE (1), the following LBE for the evolution of the microscopic distribution function, $g(\mathbf{x}, \boldsymbol{\xi}, t)$, was proposed in [13]

$$g_\alpha(\mathbf{x} + \mathbf{e}_\alpha \delta t, t + \delta t) - g_\alpha(\mathbf{x}, t) = [Lg(\mathbf{x}, t)]_\alpha + \omega_\alpha G(\mathbf{x}, t) \delta t, \quad (2)$$

where $g_\alpha(\mathbf{x}, t) \equiv g(\mathbf{x}, \boldsymbol{\xi}_\alpha, t)$, \mathbf{x} is the spatial vector, $\boldsymbol{\xi}$ is the particle velocity vector in the phase space $(\mathbf{x}, \boldsymbol{\xi})$ and it is discretized to a small set of discrete velocities $\{\boldsymbol{\xi}_\alpha | \alpha = 0, 1, \dots, 6\}$, \mathbf{e}_α is the α th discrete velocity vector $[\{\mathbf{e}_\alpha\} = (0, 0, 0), (\pm 1, 0, 0), (0, \pm 1, 0), \text{ and } (0, 0, \pm 1)$ for D3Q7 and $\{\mathbf{e}_\alpha\} = (0, 0), (\pm 1, 0), \text{ and } (0, \pm 1)$ for D2Q5], δt is the time

treatment was given in [14] as

$$g_{\bar{\alpha}}(\mathbf{x}_f, t + \delta t) = c_{n1} \hat{g}_{\bar{\alpha}}(\mathbf{x}_f, t) + c_{n2} \hat{g}_{\bar{\alpha}}(\mathbf{x}_{ff}, t) + c_{n3} \hat{g}_{\bar{\alpha}}(\mathbf{x}_f, t) + c_{n4} \frac{\delta t}{\delta x} \Phi_{n\bar{\alpha}}, \quad (10)$$

where it should be noted that $\Phi_{n\bar{\alpha}}$ is the boundary flux along the lattice velocity $\mathbf{e}_{\bar{\alpha}}$ direction. The asymptotic analysis in [14] showed that to maintain second-order accuracy, the coefficients c_{n1} - c_{n4} in Eq. (10) are uniquely determined as

$$c_{n1} = 1, \quad c_{n2} = -\frac{2\Delta - 1}{2\Delta + 1},$$

$$c_{n3} = \frac{2\Delta - 1}{2\Delta + 1}, \quad \text{and} \quad c_{n4} = \frac{2}{2\Delta + 1}. \quad (11)$$

As emphasized in [14,15], when the local boundary normal \mathbf{n} is aligned with $\mathbf{e}_{\bar{\alpha}}$, $\Phi_{n\bar{\alpha}} = \Phi_n$ and thus treatment (10) can be directly applied. When \mathbf{n} is not in the $\mathbf{e}_{\bar{\alpha}}$ direction, which is usually encountered on inclined or curved boundaries, $\Phi_{n\bar{\alpha}}$ is not equal to Φ_n and it also depends on the unknown tangential flux. A Cartesian decomposition method was proposed in [14] to conveniently and accurately obtain $\Phi_{n\bar{\alpha}}$ based on Φ_n . For details about the Neumann condition treatment for curved boundaries and its extension to mixed boundary conditions, please refer to [14].

IV. CONJUGATE CONDITION TREATMENT AT THE INTERFACE

Based on the Dirichlet and Neumann boundary condition treatments in Sec. III, an interface treatment for conjugate heat and mass transfer at the interface in the LBE method can be derived.

As illustrated in Fig. 1, the conjugate interface conditions, including the continuity of the macroscopic variable ϕ (temperature or concentration) and its normal flux at the interface, can be expressed as

$$\phi_f = \Phi_d = \phi_s \quad (12)$$

and

$$\Phi_{nf} = -D_f \frac{\partial \phi_f}{\partial n_f} = \sigma D_s \frac{\partial \phi_s}{\partial n_s} = -\sigma \Phi_{ns}, \quad (13)$$

where the indices f and s denote the two different subdomains, such as the fluid and solid phases, respectively, in conjugate heat and mass transfer on a fluid-solid interface, Φ_d is the interfacial value of ϕ , Φ_{nf} and Φ_{ns} are the normal fluxes related to the diffusivities D_f and D_s , respectively [see the diffusion coefficient in Eq. (1)], n_f and n_s are the normal vector components, and the ratio $\sigma = 1$ in mass transfer and $\sigma = (\rho c_p)_s / (\rho c_p)_f$ in heat transfer problems, with ρ being the density and c_p the heat capacity.

With the interface treated as a boundary of zero thickness for both subdomains, the following boundary treatments are readily obtained from the Dirichlet and Neumann condition treatments in Eqs. (8) and (10), respectively: Dirichlet condition,

$$g_{\bar{\alpha}}(\mathbf{x}_f, t + \delta t) = c_{d1} \hat{g}_{\bar{\alpha}}(\mathbf{x}_f, t) + c_{d2} \hat{g}_{\bar{\alpha}}(\mathbf{x}_{ff}, t) + c_{d3} \hat{g}_{\bar{\alpha}}(\mathbf{x}_f, t) + c_{d4} \varepsilon_D \Phi_d, \quad (14a)$$

$$g_{\alpha}(\mathbf{x}_s, t + \delta t) = c_{d1}^* \hat{g}_{\bar{\alpha}}(\mathbf{x}_s, t) + c_{d2}^* \hat{g}_{\bar{\alpha}}(\mathbf{x}_{ss}, t) + c_{d3}^* \hat{g}_{\bar{\alpha}}(\mathbf{x}_s, t) + c_{d4}^* \varepsilon_D \Phi_d, \quad (14b)$$

Neumann condition,

$$g_{\bar{\alpha}}(\mathbf{x}_f, t + \delta t) = c_{n1} \hat{g}_{\bar{\alpha}}(\mathbf{x}_f, t) + c_{n2} \hat{g}_{\bar{\alpha}}(\mathbf{x}_{ff}, t) + c_{n3} \hat{g}_{\bar{\alpha}}(\mathbf{x}_f, t) + c_{n4} (\delta t / \delta x) \Phi_{n\bar{\alpha}}, \quad (15a)$$

$$g_{\alpha}(\mathbf{x}_s, t + \delta t) = c_{n1}^* \hat{g}_{\bar{\alpha}}(\mathbf{x}_s, t) + c_{n2}^* \hat{g}_{\bar{\alpha}}(\mathbf{x}_{ss}, t) + c_{n3}^* \hat{g}_{\bar{\alpha}}(\mathbf{x}_s, t) + c_{n4}^* (\delta t / \delta x) \Phi_{n\alpha}, \quad (15b)$$

where $\Phi_{n\bar{\alpha}}$ and $\Phi_{n\alpha}$ are the respective interfacial fluxes along the discrete lattice velocity directions $\mathbf{e}_{\bar{\alpha}}$ and \mathbf{e}_{α} and \mathbf{x}_s and \mathbf{x}_{ss} are the first and second interior lattice nodes along the \mathbf{e}_{α} direction in Domain 2, respectively. The coefficients c_{di}^* and c_{ni}^* ($i = 1, 2, 3$, and 4) are related to c_{di} and c_{ni} as

$$c_{di}^* = c_{di}(\Delta^*) = c_{di}(1 - \Delta) \quad (16)$$

and

$$c_{ni}^* = c_{ni}(\Delta^*) = c_{ni}(1 - \Delta),$$

since the intersection fraction in Domain 2 is $\Delta^* = \|\mathbf{x}_s - \mathbf{x}_w\| / \|\mathbf{x}_f - \mathbf{x}_s\| = 1 - \Delta$.

To implement the interfacial flux condition in Eq. (13), the relationship between the flux in the lattice direction and that in the normal direction of the interface must be applied in both Domains 1 and 2. According to [14], the following relationships exist for two-dimensional (2D) cases:

$$\Phi_{n\bar{\alpha}} = \left\{ \frac{1}{c'_{d4}} [(c'_{n1} - c'_{d1}) \hat{g}_{\bar{\beta}}(\mathbf{x}'_f, t) + (c'_{n2} - c'_{d2}) \hat{g}_{\bar{\beta}}(\mathbf{x}'_{ff}, t) + (c'_{n3} - c'_{d3}) \hat{g}_{\bar{\beta}}(\mathbf{x}'_f, t)] \sin \theta - \frac{1}{c_{d4}} [(c_{n1} - c_{d1}) \hat{g}_{\bar{\alpha}}(\mathbf{x}_f, t) + (c_{n2} - c_{d2}) \hat{g}_{\bar{\alpha}}(\mathbf{x}_{ff}, t) + (c_{n3} - c_{d3}) \hat{g}_{\bar{\alpha}}(\mathbf{x}_f, t)] \sin \theta + \frac{c'_{n4}}{c'_{d4}} \frac{\delta t}{\delta x} \Phi_{nf} \right\} / \left[\frac{c_{n4}}{c_{d4}} \frac{\delta t}{\delta x} \sin \theta + \frac{c'_{n4}}{c'_{d4}} \frac{\delta t}{\delta x} \cos \theta \right], \quad (17a)$$

$$\Phi_{n\alpha} = \left\{ \frac{1}{c'_{d4}} [(c'_{n1} - c'_{d1}) \hat{g}_{\bar{\beta}}(\mathbf{x}'_s, t) + (c'_{n2} - c'_{d2}) \hat{g}_{\bar{\beta}}(\mathbf{x}'_{ss}, t) + (c'_{n3} - c'_{d3}) \hat{g}_{\bar{\beta}}(\mathbf{x}'_s, t)] \sin \theta - \frac{1}{c_{d4}^*} [(c_{n1}^* - c_{d1}^*) \hat{g}_{\bar{\alpha}}(\mathbf{x}_s, t) + (c_{n2}^* - c_{d2}^*) \hat{g}_{\bar{\alpha}}(\mathbf{x}_{ss}, t) + (c_{n3}^* - c_{d3}^*) \hat{g}_{\bar{\alpha}}(\mathbf{x}_s, t)] \sin \theta + \frac{c'_{n4}}{c'_{d4}} \frac{\delta t}{\delta x} \Phi_{ns} \right\} / \left[\frac{c_{n4}^*}{c_{d4}^*} \frac{\delta t}{\delta x} \sin \theta + \frac{c'_{n4}}{c'_{d4}} \frac{\delta t}{\delta x} \cos \theta \right], \quad (17b)$$

where θ is the angle between the lattice vector $\mathbf{e}_{\bar{\alpha}}$ and the normal \mathbf{n} at the interface node \mathbf{x}_w , $\hat{g}_{\bar{\beta}}$ and \hat{g}_{β} are the postcollision distribution functions along the lattice directions $\mathbf{e}_{\bar{\beta}}$ and \mathbf{e}_{β} that are perpendicular to $\mathbf{e}_{\bar{\alpha}}$ and \mathbf{e}_{α} , and they are evaluated at the intersection nodes $\mathbf{x}'_f = \mathbf{x}'_s = \mathbf{x}_w$, $\mathbf{x}'_{ff} = \mathbf{x}_w + \mathbf{e}_{\bar{\beta}} \delta t$, and $\mathbf{x}'_{ss} = \mathbf{x}_w + \mathbf{e}_{\beta} \delta t$ (see Fig. 1), with interpolation or extrapolation of the neighboring distribution functions. Specifically, the distributions $\hat{g}_{\bar{\beta}}$ and \hat{g}_{β} at \mathbf{x}'_f in Domain 1 are obtained from a quadratic extrapolation of the respective distributions $\hat{g}_{\bar{\beta}}$ and \hat{g}_{β} at the three neighboring nodes in Domain 1, and \hat{g}_{β} at \mathbf{x}'_{ff} is obtained from a quadratic interpolation or extrapolation of the three neighboring nodes in Domain 1 depending on whether \mathbf{x}'_{ff} is located between two nodes in Domain 1 or between a

node in Domain 1 and an interface node, respectively. The same procedure applies to the evaluation of \hat{g}_β and \hat{g}_β in Domain 2 as well. The coefficients c'_{di} and c'_{ni} ($i = 1, 2, 3$, and 4) are determined from Eqs. (9) and (11) by setting $\Delta = 0$; i.e.,

$$c'_{di} = c_{di}(\Delta') = c_{di}(\Delta = 0) \quad (18)$$

$$\text{and} \quad c'_{ni} = c_{ni}(\Delta') = c_{ni}(\Delta = 0).$$

A. General conjugate interface treatment

The combination of Eqs. (14a) and (14b) gives one equation for the two unknowns $g_{\bar{\alpha}}(\mathbf{x}_f, t + \delta t)$ and $g_{\alpha}(\mathbf{x}_s, t + \delta t)$. Substituting Eqs. (17a) and (17b) into Eqs. (15a) and (15b) and recalling the relationship in Eq. (13), one obtains another equation for these unknowns. The solutions to the equations are

$$\begin{aligned} g_{\bar{\alpha}}(\mathbf{x}_f, t + \delta t) &= A_1^f \hat{g}_{\alpha}(\mathbf{x}_f, t) + A_2^f \hat{g}_{\alpha}(\mathbf{x}_{ff}, t) + A_3^f \hat{g}_{\bar{\alpha}}(\mathbf{x}_f, t) \\ &\quad + B_1^f \hat{g}_{\bar{\alpha}}(\mathbf{x}_s, t) + B_2^f \hat{g}_{\bar{\alpha}}(\mathbf{x}_{ss}, t) + B_3^f \hat{g}_{\alpha}(\mathbf{x}_s, t) \\ &\quad + C_1^f \hat{g}_{\beta}(\mathbf{x}'_f, t) + C_2^f \hat{g}_{\beta}(\mathbf{x}'_{ff}, t) + C_3^f \hat{g}_{\bar{\beta}}(\mathbf{x}'_f, t) \\ &\quad + \sigma C_1^f \hat{g}_{\bar{\beta}}(\mathbf{x}'_s, t) + \sigma C_2^f \hat{g}_{\bar{\beta}}(\mathbf{x}'_{ss}, t) + \sigma C_3^f \hat{g}_{\beta}(\mathbf{x}'_s, t), \end{aligned} \quad (19a)$$

$$\begin{aligned} g_{\alpha}(\mathbf{x}_s, t + \delta t) &= A_1^s \hat{g}_{\bar{\alpha}}(\mathbf{x}_s, t) + A_2^s \hat{g}_{\bar{\alpha}}(\mathbf{x}_{ss}, t) + A_3^s \hat{g}_{\alpha}(\mathbf{x}_s, t) \\ &\quad + B_1^s \hat{g}_{\alpha}(\mathbf{x}_f, t) + B_2^s \hat{g}_{\alpha}(\mathbf{x}_{ff}, t) + B_3^s \hat{g}_{\bar{\alpha}}(\mathbf{x}_f, t) \\ &\quad + \sigma C_1^s \hat{g}_{\bar{\beta}}(\mathbf{x}'_s, t) + \sigma C_2^s \hat{g}_{\bar{\beta}}(\mathbf{x}'_{ss}, t) + \sigma C_3^s \hat{g}_{\beta}(\mathbf{x}'_s, t) \\ &\quad + C_1^s \hat{g}_{\beta}(\mathbf{x}'_f, t) + C_2^s \hat{g}_{\beta}(\mathbf{x}'_{ff}, t) + C_3^s \hat{g}_{\bar{\beta}}(\mathbf{x}'_f, t), \end{aligned} \quad (19b)$$

where the coefficients are determined from

$$\begin{aligned} A_i^f &= \left[\frac{(\sigma + 1)c'_{d4}c_{di}}{c_{d4}c_{d4}^*c'_{n4}} \sin \theta + \left(\frac{\sigma c_{di}}{c_{d4}c_{n4}^*} + \frac{c_{ni}}{c_{d4}^*c_{n4}} \right) \cos \theta \right] / P, \\ B_i^f &= \sigma \left(\frac{c_{ni}^* - c_{di}^*}{c_{d4}^*c_{n4}^*} \right) \cos \theta / P, \\ C_i^f &= \left(\frac{c'_{d4}}{c_{d4}^*c'_{n4}} \frac{c'_{ni} - c'_{di}}{c'_{d4}} \right) \sin \theta / P, \quad (i = 1, 2, 3) \end{aligned} \quad (20a)$$

and

$$\begin{aligned} A_i^s &= \left[\frac{(1 + \sigma)c'_{d4}c_{di}^*}{c_{d4}^*c_{d4}c'_{n4}} \sin \theta + \left(\frac{c_{di}^*}{c_{d4}^*c_{n4}} + \frac{\sigma c_{ni}^*}{c_{d4}c_{n4}^*} \right) \cos \theta \right] / P, \\ B_i^s &= \left(\frac{c_{ni} - c_{di}}{c_{d4}c_{n4}} \right) \cos \theta / P, \\ C_i^s &= \left(\frac{c'_{d4}}{c_{d4}c'_{n4}} \frac{c'_{ni} - c'_{di}}{c'_{d4}} \right) \sin \theta / P, \quad (i = 1, 2, 3) \end{aligned} \quad (20b)$$

with

$$P = \frac{(\sigma + 1)c'_{d4}}{c_{d4}c_{d4}^*c'_{n4}} \sin \theta + \left(\frac{\sigma}{c_{d4}c_{n4}^*} + \frac{1}{c_{d4}^*c_{n4}} \right) \cos \theta. \quad (21)$$

The present general interface treatment in Eqs. (19a) and (19b) can be directly applied to curved interface

simulations since the local geometry of the interface is preserved by using the precise values of the local link fraction Δ and the angle θ between the interfacial normal \mathbf{n} and the lattice vector $\mathbf{e}_{\bar{\alpha}}$. The coefficients c_{di} , c_{ni} , c_{di}^* , c_{ni}^* , c'_{di} , and c'_{ni} ($i = 1-4$) in Eqs. (20a), (20b), and (21) are also related to the local Δ as given in Eqs. (9), (11), (16), and (18).

With $g_{\bar{\alpha}}(\mathbf{x}_f, t + \delta t)$ and $g_{\alpha}(\mathbf{x}_s, t + \delta t)$ obtained from the present conjugate interface treatment, the macroscopic value ϕ and its fluxes in the lattice velocity directions $\mathbf{e}_{\bar{\alpha}}$ and \mathbf{e}_{α} at the interface can be solved according to Eqs. (14a), (14b) and (15a), (15b). Those evaluation schemes are rewritten as

$$\begin{aligned} \Phi_d &= \frac{1}{c_{d4}\varepsilon_D} [g_{\bar{\alpha}}(\mathbf{x}_f, t + \delta t) - c_{d1}\hat{g}_{\alpha}(\mathbf{x}_f, t) \\ &\quad - c_{d2}\hat{g}_{\alpha}(\mathbf{x}_{ff}, t) - c_{d3}\hat{g}_{\bar{\alpha}}(\mathbf{x}_f, t)] \end{aligned} \quad (22a)$$

or

$$\begin{aligned} \Phi_d &= \frac{1}{c_{d4}^*\varepsilon_D} [g_{\alpha}(\mathbf{x}_s, t + \delta t) - c_{d1}^*\hat{g}_{\bar{\alpha}}(\mathbf{x}_s, t) \\ &\quad - c_{d2}^*\hat{g}_{\bar{\alpha}}(\mathbf{x}_{ss}, t) - c_{d3}^*\hat{g}_{\alpha}(\mathbf{x}_s, t)], \end{aligned} \quad (22b)$$

$$\begin{aligned} \Phi_{n\bar{\alpha}} &= \frac{\delta x}{c_{n4}\delta t} [g_{\bar{\alpha}}(\mathbf{x}_f, t + \delta t) - c_{n1}\hat{g}_{\alpha}(\mathbf{x}_f, t) \\ &\quad - c_{n2}\hat{g}_{\alpha}(\mathbf{x}_{ff}, t) - c_{n3}\hat{g}_{\bar{\alpha}}(\mathbf{x}_f, t)], \end{aligned} \quad (23a)$$

and

$$\begin{aligned} \Phi_{n\alpha} &= \frac{\delta x}{c_{n4}^*\delta t} [g_{\alpha}(\mathbf{x}_s, t + \delta t) - c_{n1}^*\hat{g}_{\bar{\alpha}}(\mathbf{x}_s, t) \\ &\quad - c_{n2}^*\hat{g}_{\bar{\alpha}}(\mathbf{x}_{ss}, t) - c_{n3}^*\hat{g}_{\alpha}(\mathbf{x}_s, t)]. \end{aligned} \quad (23b)$$

It is worth mentioning that there are special situations, such as straight interface cases and those with zero-tangential fluxes along the interface, for which the present conjugate interface treatment can be greatly simplified by decoupling the interfacial fluxes along the lattice velocity directions. The decoupled interface treatment is thus presented in the next section.

B. Decoupled conjugate interface treatment

For conjugate heat and mass transfer at straight interfaces, it is natural to place the lattice in such a way that the lattice vectors $\mathbf{e}_{\bar{\alpha}}$ and \mathbf{e}_{α} are aligned with the normal \mathbf{n} of the interface; thus, the following relationships are readily obtained:

$$\Phi_{n\bar{\alpha}} = \Phi_{nf} \quad \text{and} \quad \Phi_{n\alpha} = \Phi_{ns}, \quad \text{when} \quad \mathbf{e}_{\bar{\alpha}} // \mathbf{n}. \quad (24)$$

When the tangential flux Φ_t along an interface is known to be zero, such as that in axisymmetric problems, the simple projection rule holds (see Fig. 1):

$$\Phi_{n\bar{\alpha}} = \Phi_{nf} \cos \theta \quad \text{and} \quad \Phi_{n\alpha} = \Phi_{ns} \cos \theta, \quad \text{when} \quad \Phi_t = 0. \quad (25)$$

Clearly for these two cases, the coupling of the interfacial fluxes in the lattice velocity directions $\mathbf{e}_{\bar{\alpha}}$ and \mathbf{e}_{β} can be eliminated. By replacing Eqs. (17a) and (17b) with the decoupled relationships in either Eq. (24) or (25) the conjugate interface treatment in Eqs. (19a) and (19b) is simplified to

$$\begin{aligned} g_{\bar{\alpha}}(\mathbf{x}_f, t + \delta t) &= A_1^f \hat{g}_{\alpha}(\mathbf{x}_f, t) + A_2^f \hat{g}_{\alpha}(\mathbf{x}_{ff}, t) + A_3^f \hat{g}_{\bar{\alpha}}(\mathbf{x}_f, t) \\ &\quad + B_1^f \hat{g}_{\bar{\alpha}}(\mathbf{x}_s, t) + B_2^f \hat{g}_{\bar{\alpha}}(\mathbf{x}_{ss}, t) + B_3^f \hat{g}_{\alpha}(\mathbf{x}_s, t), \end{aligned} \quad (26a)$$

$$\begin{aligned}
 g_\alpha(\mathbf{x}_s, t + \delta t) &= A_1^s \hat{g}_\alpha(\mathbf{x}_s, t) + A_2^s \hat{g}_\alpha(\mathbf{x}_{ss}, t) + A_3^s \hat{g}_\alpha(\mathbf{x}_s, t) \\
 &\quad + B_1^s \hat{g}_\alpha(\mathbf{x}_f, t) + B_2^s \hat{g}_\alpha(\mathbf{x}_{ff}, t) + B_3^s \hat{g}_\alpha(\mathbf{x}_f, t),
 \end{aligned} \tag{26b}$$

with

$$\begin{aligned}
 A_i^f &= \left(\frac{\sigma c_{di}}{c_{d4} c_{n4}^*} + \frac{c_{ni}}{c_{d4}^* c_{n4}} \right) / P, \\
 B_i^f &= \sigma \left(\frac{c_{ni}^* - c_{di}^*}{c_{d4}^* c_{n4}^*} \right) / P, \\
 A_i^s &= \left(\frac{c_{di}^*}{c_{d4}^* c_{n4}^*} + \frac{\sigma c_{ni}^*}{c_{d4} c_{n4}} \right) / P, \\
 B_i^s &= \left(\frac{c_{ni} - c_{di}}{c_{d4} c_{n4}} \right) / P, \quad (i = 1, 2, 3)
 \end{aligned} \tag{27a}$$

and

$$P = \frac{\sigma}{c_{d4} c_{n4}^*} + \frac{1}{c_{d4}^* c_{n4}}. \tag{27b}$$

C. Present particular conjugate interface schemes

Three particular boundary schemes (see Appendix B) for Dirichlet conditions were presented in [14] with different choices of the adjustable coefficient c_{d1} in Eq. (8) as a function of the local Δ value. Their numerical stability and second-order accuracy were also examined and verified in [14]. Since c_{d1} is also the adjustable coefficient in the present interface treatment in Eqs. (19a) and (19b) when the relationships in Eqs. (9), (11), (16), and (18) for the other coefficients are preserved for second-order accuracy, three particular conjugate interface schemes are explicitly provided in this work. Their specific coefficients for 2D problems are listed in Table I.

For the decoupled interface treatment in Eqs. (26a) and (26b), three corresponding particular schemes are also obtained. Their coefficients in Eqs. (27a) and (27b) can be simplified from Table I with a direct substitution of $\sin\theta = 0$ and $\cos\theta = 1$. For convenience, the coefficients are listed separately in Table II.

D. The modified ‘‘half-lattice division’’ interface treatment

In the previous conjugate interface schemes used in [9–11, 16], the interfaces are straight and located ‘‘halfway’’ between the lattice nodes ($\Delta = 0.5$). With the substitution of $\Delta = 0.5$ in Table II, the decoupled conjugate treatment in Eqs. (26a) and (26b) becomes

$$g_{\bar{\alpha}}(\mathbf{x}_f, t + \delta t) = \left(\frac{1 - \sigma}{1 + \sigma} \right) \hat{g}_\alpha(\mathbf{x}_f, t) + \left(\frac{2\sigma}{1 + \sigma} \right) \hat{g}_{\bar{\alpha}}(\mathbf{x}_s, t), \tag{28a}$$

$$g_\alpha(\mathbf{x}_s, t + \delta t) = - \left(\frac{1 - \sigma}{1 + \sigma} \right) \hat{g}_{\bar{\alpha}}(\mathbf{x}_s, t) + \left(\frac{2}{1 + \sigma} \right) \hat{g}_\alpha(\mathbf{x}_f, t). \tag{28b}$$

In each of the above equations, the first term on the right side represents the bounce-back contribution at the interface and the second term represents the streaming or transport contribution from one phase to the other crossing over the interface. It is also noticed that only the local distributions at \mathbf{x}_f and \mathbf{x}_s are

required in this modified half-lattice division (HLD) scheme. Furthermore, for the most simplified case of $\Delta = 0.5$ and $\sigma = 1$, the modified HLD scheme reduces to

$$g_{\bar{\alpha}}(\mathbf{x}_f, t + \delta t) = \hat{g}_{\bar{\alpha}}(\mathbf{x}_s, t), \tag{29a}$$

$$g_\alpha(\mathbf{x}_s, t + \delta t) = \hat{g}_\alpha(\mathbf{x}_f, t). \tag{29b}$$

Equations (29a) and (29b) show that no special treatment is needed for the nodes in Domains 1 and 2 adjacent to the interface. The standard streaming step in Eq. (7) can be directly applied to the interior lattice nodes surrounding the interface. This is the algorithm used in the previous studies in [9–11, 16].

According to the asymptotic analysis for boundary conditions in [14], the HLD scheme in Eqs. (29a) and (29b) is first-order accurate in general and it has second-order accuracy only for the special case of $\Delta = 0.5$. On the contrary, the presently proposed decoupled interface schemes in Eqs. (26a) and (26b) with the coefficients determined in Eqs. (27a) and (27b) are able to preserve second-order accuracy for arbitrary Δ values. For curved interfaces with nonzero tangential fluxes, the accuracy of the general interface treatment in Eqs. (19a) and (19b) is affected by the curved geometry. Based on the convergence observations in [14, 15] for curved boundary simulations, the present interface treatment for curved interfaces should be able to preserve second-order accuracy for the temperature (concentration) field and first-order accuracy for their interfacial fluxes. The accuracy of these interface schemes are verified with numerical examples in Sec. V.

V. NUMERICAL VERIFICATION

Four numerical tests are conducted in this section to verify the applicability and accuracy of the proposed conjugate interface treatment. Tests (i) and (ii) study the steady-state and transient convection-diffusion in a 2D channel containing two different fluids, respectively. The interface in the channel is straight and perpendicular to one of the discrete lattice velocities so that the decoupled conjugate schemes are applied. The interface is placed at different locations between two layers of lattice nodes to elucidate the effect of the link fraction Δ value on the accuracy of the conjugate schemes. Curved interfaces are encountered in the last two tests, where test (iii) simulates the steady-state heat conduction within a circular domain of two solids, and test (iv) is for conjugate mass transfer simulation between a spherical droplet and the surrounding fluid. For tests (iii) and (iv), the interfacial fluxes in different directions are fully coupled; thus, the general interface treatment must be employed. Analytical solutions are available for tests (i) to (iii) so that the numerical accuracy of the interface treatment is fully examined in terms of the simulated interior temperature (concentration) field, the macroscopic interfacial values and the interfacial fluxes. The computed Sherwood numbers for conjugate mass transfer in test (iv) are compared with published results in [8]. It should be noted that in each of those tests, the velocity field is prescribed and not coupled with the heat or mass transfer. The Dirichlet and Neumann boundary conditions proposed in [14], which are the basis for the present conjugate interface treatment, can be extended to the mixed or ‘‘third-type’’ boundary condition as demonstrated in [14] and their coupling with hydrodynamic

TABLE I. Coefficients in Schemes 1, 2, and 3 for the general conjugate interface treatment in Eqs. (19a) and (19b) for 2D simulations.

	Scheme 1 ($0 \leq \Delta \leq 0.5$)	Scheme 1 ($0.5 < \Delta \leq 1$)	Scheme 2 ($0 \leq \Delta \leq 1$)	Scheme 3 ($0 \leq \Delta \leq 1$)
A_1^f	$\{-2\Delta(1-\Delta)(\sigma+1)\sin\theta + [-\Delta(3-2\Delta)\sigma + (1-\Delta)(2\Delta+1)\cos\theta]/P$	$[-\frac{\sigma+1}{2}\sin\theta + (-\frac{3-2\Delta}{2}\sigma + \frac{2\Delta+1}{2})\cos\theta]/P$	$\{-3(1-\Delta)(\sigma+1)\sin\theta + [3-\frac{2\Delta}{2} - (1-\Delta)(2\Delta+1)\sigma]\cos\theta\}/P$	$-(2\Delta+1)(3-2\Delta)[\frac{(\sigma+1)\sin\theta + (\sigma-1)\cos\theta}{P}]$
A_2^f	$(2\Delta-1)\{(1-\Delta)(\sigma+1)\sin\theta + [3-\frac{2\Delta}{2}\sigma - (1-\Delta)\cos\theta\}/P$	$(\frac{1-2\Delta}{2})\cos\theta/P$	$(1-2\Delta)\{\frac{3(2\Delta-1)}{2(2\Delta+1)}(\sigma+1)\sin\theta + [\frac{3-2\Delta}{2(2\Delta+1)} - \frac{1-2\Delta}{2}\sigma]\cos\theta\}/P$	$(2\Delta-1)(3-2\Delta)[\frac{(\sigma+1)\sin\theta + (\sigma-1)\cos\theta}{P}]$
A_3^f	$(1-\Delta)(2\Delta-1)\cos\theta/P$	$(2\Delta-1)[\frac{\sigma+1}{2}\sin\theta + (\frac{3-2\Delta}{2}\sigma + \frac{1}{2})\cos\theta]/P$	$(2\Delta-1)\{\frac{3}{2\Delta+1}(\sigma+1)\sin\theta + [\frac{3-2\Delta}{2(2\Delta+1)} + \sigma]\cos\theta\}/P$	$(2\Delta-1)(3-2\Delta)[\frac{(\sigma+1)\sin\theta + (\sigma-1)\cos\theta}{P}]$
B_1^f	$\frac{(3-2\Delta)^2}{2}\sigma\cos\theta/P$	$\frac{(3-2\Delta)^2}{2}\sigma\cos\theta/P$	$\frac{(3-2\Delta)^2}{2}\sigma\cos\theta/P$	$2(3-2\Delta)^2\sigma\cos\theta/P$
B_2^f	$(1-\Delta)(2\Delta-1)\sigma\cos\theta/P$	$(2-\Delta)(2\Delta-1)\sigma\cos\theta/P$	$\frac{\Delta(2\Delta-1)(3-2\Delta)}{2\Delta+1}\sigma\cos\theta/P$	$2(2\Delta-1)(3-2\Delta)\sigma\cos\theta/P$
B_3^f	$(\frac{2\Delta-1}{2})\sigma\cos\theta/P$	$(\frac{1-2\Delta}{2})\sigma\cos\theta/P$	$\frac{(2\Delta-1)(3-2\Delta)}{2(2\Delta+1)}\sigma\cos\theta/P$	0
C_1^f	$(1-\Delta)\sin\theta/P$	$\frac{1}{2}\sin\theta/P$	$\frac{3(3-2\Delta)}{2(2\Delta+1)}\sin\theta/P$	$2(3-2\Delta)\sin\theta/P$
C_2^f	$2(1-\Delta)\sin\theta/P$	$\sin\theta/P$	$\frac{3-2\Delta}{2\Delta+1}\sin\theta/P$	$2(3-2\Delta)\sin\theta/P$
C_3^f	$-(1-\Delta)\sin\theta/P$	$-\frac{1}{2}\sin\theta/P$	$\frac{3-2\Delta}{2(2\Delta+1)}\sin\theta/P$	0
A_1^s	$[-\frac{\sigma+1}{2}\sin\theta + (\frac{3-2\Delta}{2}\sigma - \frac{2\Delta+1}{2})\cos\theta]/P$	$\{-2\Delta(1-\Delta)(\sigma+1)\sin\theta + [\Delta(3-2\Delta)\sigma - (1-\Delta)(2\Delta+1)]\cos\theta\}/P$	$\{-3\Delta(\sigma+1)\sin\theta + [\frac{2\Delta+1}{2}\sigma - \Delta(3-2\Delta)]\cos\theta\}/P$	$-(3-2\Delta)(2\Delta+1)[\frac{(\sigma+1)\sin\theta + (1-\sigma)\cos\theta}{P}]$
A_2^s	$(\frac{2\Delta-1}{2})\sigma\cos\theta/P$	$(1-2\Delta)[\Delta(\sigma+1)\sin\theta + (-\Delta\sigma + \frac{2\Delta+1}{2})\cos\theta]/P$	$(2\Delta-1)\{\frac{3(1-2\Delta)}{2(3-2\Delta)}(\sigma+1)\sin\theta + [\frac{2\Delta+1}{2(3-2\Delta)}\sigma - \frac{2\Delta-1}{2}]\cos\theta\}/P$	$(1-2\Delta)(2\Delta+1)[\frac{(\sigma+1)\sin\theta + (1-\sigma)\cos\theta}{P}]$
A_3^s	$(1-2\Delta)[\frac{\sigma+1}{2}\sin\theta + (\frac{\sigma}{2} + \frac{2\Delta+1}{2}\cos\theta)]/P$	$\Delta(1-2\Delta)\sigma\cos\theta/P$	$(1-2\Delta)\{\frac{3}{3-2\Delta}(\sigma+1)\sin\theta + [\frac{2\Delta+1}{2(3-2\Delta)}\sigma + 1]\cos\theta\}/P$	$(1-2\Delta)(2\Delta+1)[\frac{(\sigma+1)\sin\theta + \cos\theta}{P}]$
B_1^s	$\frac{(2\Delta+1)^2}{2}\cos\theta/P$	$\frac{(2\Delta+1)^2}{2}\cos\theta/P$	$\frac{(2\Delta+1)^2}{2}\cos\theta/P$	$2(2\Delta+1)^2\cos\theta/P$
B_2^s	$\Delta(2\Delta-1)\cos\theta/P$	$\Delta(1-2\Delta)\cos\theta/P$	$\frac{(1-\Delta)(1-2\Delta)(2\Delta+1)}{3-2\Delta}\cos\theta/P$	$2(1-2\Delta)(2\Delta+1)\cos\theta/P$
B_3^s	$(\frac{2\Delta-1}{2})\cos\theta/P$	$(\frac{1-2\Delta}{2})\cos\theta/P$	$\frac{(1-2\Delta)(2\Delta+1)}{2(3-2\Delta)}\cos\theta/P$	0
C_1^s	$\frac{1}{2}\sin\theta/P$	$\Delta\sin\theta/P$	$\frac{3(2\Delta+1)}{2(3-2\Delta)}\sin\theta/P$	$2(2\Delta+1)\sin\theta/P$
C_2^s	$\sin\theta/P$	$2\Delta\sin\theta/P$	$\frac{2\Delta+1}{3-2\Delta}\sin\theta/P$	$2(2\Delta+1)\sin\theta/P$
C_3^s	$-\frac{1}{2}\sin\theta/P$	$-\Delta\sin\theta/P$	$\frac{2\Delta+1}{2(3-2\Delta)}\sin\theta/P$	0
P	$(1-\Delta)(\sigma+1)\sin\theta + [(3-2\Delta)\sigma/2 + (1-\Delta)(1+2\Delta)]\cos\theta$	$\Delta(\sigma+1)\sin\theta + [\Delta(3-2\Delta)\sigma + (2\Delta+1)/2]\cos\theta$	$(3/2)(\sigma+1)\sin\theta + (\frac{2\Delta+1}{2}\sigma + \frac{3-2\Delta}{2})\cos\theta$	$(2\Delta+1)(3-2\Delta)(\sigma+1)(\sin\theta + \cos\theta)$

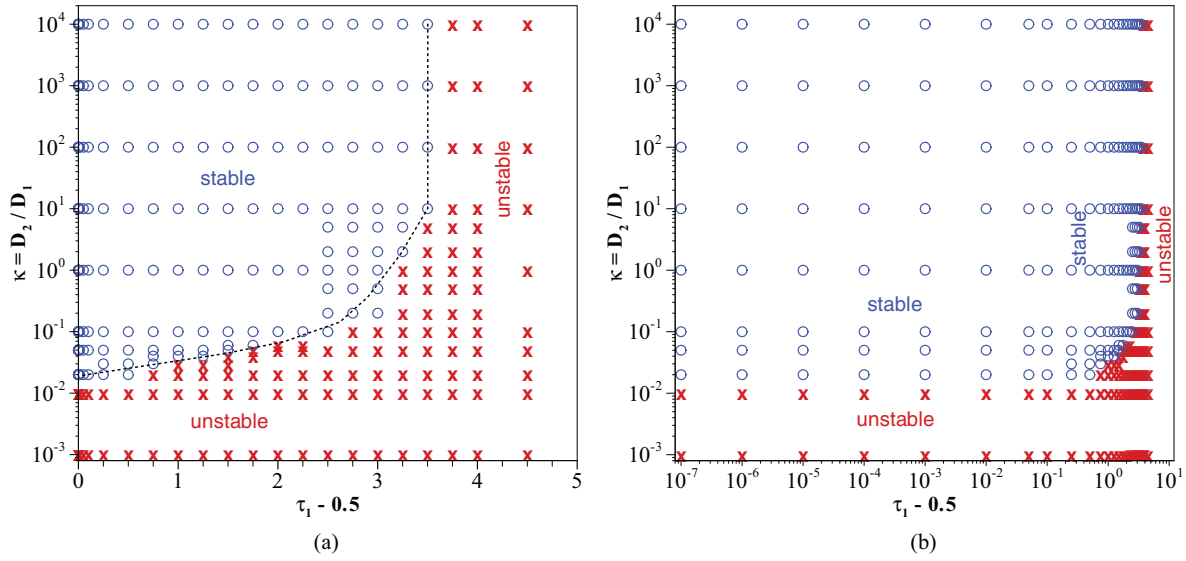


FIG. 3. (Color online) Regions of stability and instability in the LBE computation for steady convection-diffusion in the channel for various fluid diffusivity ratios $\kappa = D_2/D_1$ using different relaxation coefficient τ_1 values (a) on log-linear scale and (b) on log-log scale.

Equations (32) and (33) constitute the conjugate conditions at the interface. Again, $\sigma = 1$ in mass transfer and $\sigma = (\rho c_p)_2/(\rho c_p)_1$ in heat transfer problems can be enforced. The analytical solutions for $\phi_{1,2}$ are

$$\phi_{ex,1}(x,y) = \text{Re}\{e^{ikx}[\gamma_1 e^{-\lambda_1 y} + (1 - \gamma_1)e^{\lambda_1 y}]\} \quad (0 \leq y \leq h), \quad (34)$$

$$\phi_{ex,2}(x,y) = \text{Re}\{e^{ikx}[\gamma_2 e^{-\lambda_2 y} + (1 - \gamma_2)e^{-\lambda_2 H}]\} \quad (h \leq y \leq H), \quad (35)$$

where

$$\gamma_1 = \frac{\lambda_1 (a_3^2 - a_2^2) + \kappa \sigma \lambda_2 (2a_1 a_2 a_3 - a_2^2 - a_3^2)}{(\lambda_1 + \kappa \sigma \lambda_2) (a_1^2 a_3^2 - a_2^2) - (\lambda_1 - \kappa \sigma \lambda_2) (a_1^2 a_2^2 - a_3^2)}, \quad (36)$$

$$\gamma_2 = \frac{\lambda_1 (a_1^2 a_3 + a_3 - 2a_1 a_2) + \kappa \sigma \lambda_2 (a_1^2 - 1)}{(\lambda_1 + \kappa \sigma \lambda_2) (a_1^2 a_3^2 - a_2^2) - (\lambda_1 - \kappa \sigma \lambda_2) (a_1^2 a_2^2 - a_3^2)}, \quad (37)$$

and

$$a_1 = e^{-\lambda_1 h}, \quad a_2 = e^{-\lambda_2 h}, \quad \text{and} \quad a_3 = e^{-\lambda_2 H}. \quad (38)$$

In the above, “Re” denotes the real part of a complex number, $\kappa = D_2/D_1$ is the diffusivity ratio, and $\lambda_{1,2} = k\sqrt{1 + \frac{iU}{D_{1,2}k}}$.

The decoupled interface treatment in Eqs. (26a) and (26b) is applied since the normal of the interface is aligned with the lattice velocity vectors $\mathbf{e}_{\bar{\alpha}}$ and \mathbf{e}_{α} (see Fig. 2). The three particular interface schemes whose coefficients are listed in Table II are implemented and the corresponding Dirichlet schemes for the channel walls are also used; i.e., the same expression for the adjustable coefficient c_{d1} is used in both the interface and the wall boundary schemes. For brevity, the

basic case with $H = 2h$ and $\sigma = 1$ is studied in this section for steady-state solutions.

The numerical stability of the present conjugate interface treatment is first examined following the tests in [14,21] for boundary scheme analysis. It is well known that $\tau_1 > 0.5$ is required for stable computation of single phase problems and for positive diffusivity coefficient. Figure 3 shows the stable and unstable regions based on a large number of the computational runs with large ranges of diffusivity ratios $\kappa = D_2/D_1$ and relaxation coefficient τ_1 values. The conjugate interface Scheme 2 is used in Fig. 3 and the simulation parameters are $\text{Pe} = 20$, $H = 32\delta y$, and $\Delta = 0.0001$. Very close results for using Schemes 1 and 3 and other parameters $\text{Pe} = 50, 100$, and $\Delta = 0.9999$ are also obtained, indicating

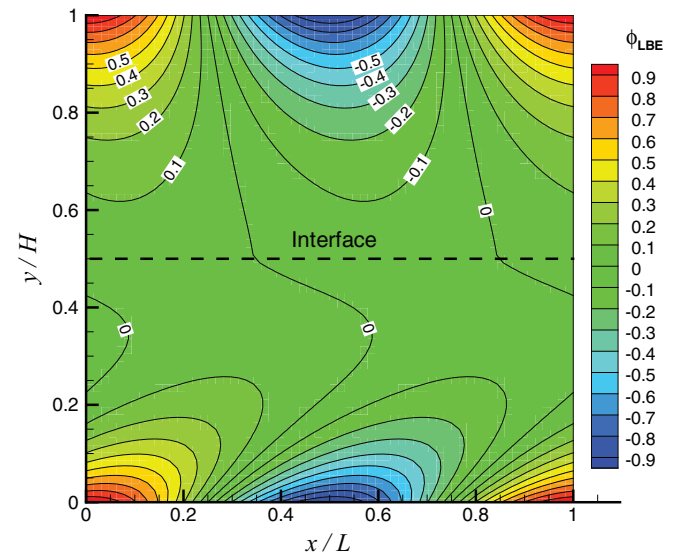


FIG. 4. (Color online) Contours of ϕ for steady convection-diffusion in the channel at $\text{Pe} = 20$ with simulation parameters $H = 2h = 64\delta y$, $\Delta = 0.5$, $\kappa = 10$, $\tau_1 = 0.55$, and $\tau_2 = 1.0$.

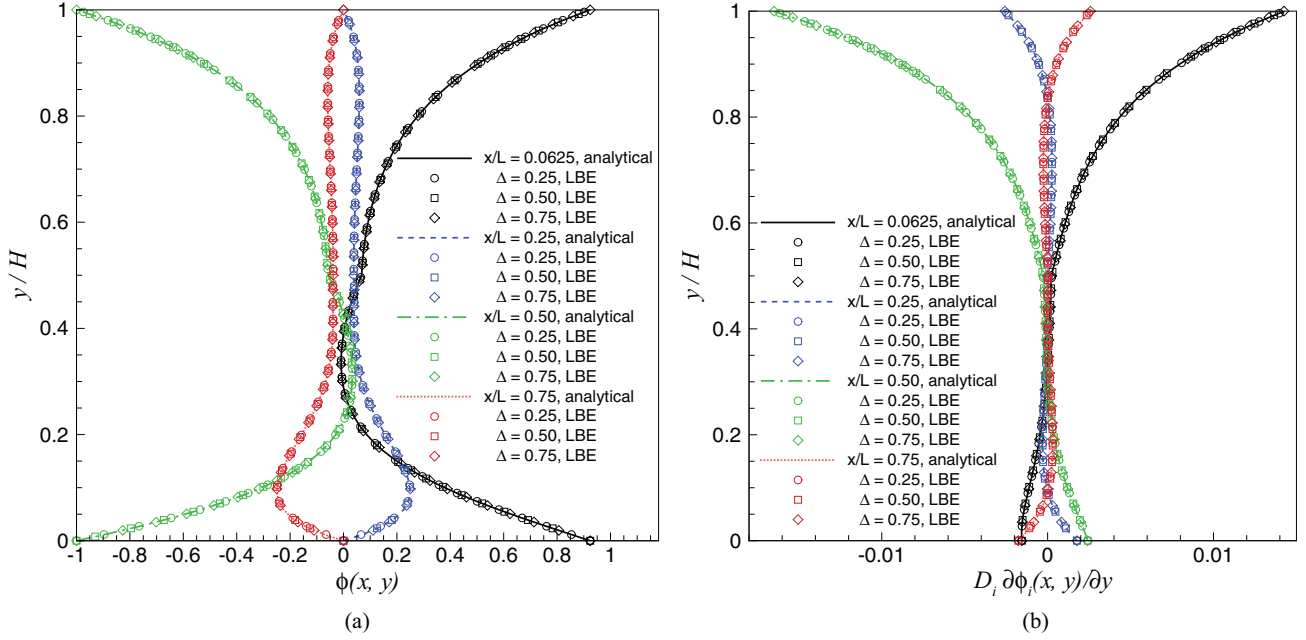


FIG. 5. (Color online) Profiles of (a) $\phi(x, y)$ and (b) $D_i \partial \phi_i / \partial y$ along vertical lines in the channel at $Pe = 20$ with $H = 2h = 64\delta y$, $\kappa = 10$, $\tau_1 = 0.55$, and $\tau_2 = 1.0$.

that the numerical stability of the present conjugate interface schemes is not sensitive to the Δ values. The region of stability shown in Fig. 3 also imply that the conjugate interface schemes are stable over a wide range of diffusivity ratios when τ_1 is in the range of $0.5 < \tau_1 \leq 4.0$, even when τ_1 is very close to 0.5.

For illustration purposes, Fig. 4 shows the contours of ϕ in the channel from the LBE simulations for $\kappa = D_2/D_1 = 10$ and $Pe = 20$ using $H = 64\delta y$, $\Delta = 0.5$, $\tau_1 = 0.55$, and $\tau_2 = 1.0$. The profiles of ϕ and its flux $D_i \partial \phi_i / \partial y$ (the subscript i denotes the subdomains) along the vertical lines at $x/L = 0.0625, 0.25, 0.50$, and 0.75 are presented in Figs. 5(a) and 5(b), respectively. In addition, both the quantity ϕ and its flux at the interface are shown in Fig. 6. Very good agreement between simulated

results and analytical solutions is obtained in Figs. 5 and 6 for each Δ value tested. It is emphasized that with the present conjugate interface treatment, the interfacial values of ϕ and its fluxes in the lattice velocity directions at the interface evaluated from the distribution functions in each subdomain are exactly the same. Identically same numerical results for $\phi(x, y = h)$ are obtained from using Eqs. (22a) and (22b), and the same numerical results for $D_i \partial \phi_i / \partial y(x, y = h)$ are obtained based on Eqs. (23a) and (23b). This has been numerically verified for all cases in the present work.

To further assess the accuracy of the interface schemes, the following L_2 norm errors are defined:

$$E_2 = \left[\frac{\sum_{x,y} (\phi_{\text{LBE}} - \phi_{\text{ex}})^2}{\sum_{x,y} \phi_{\text{ex}}^2} \right]^{1/2}, \quad (39)$$

$$E_{2,\text{tint}} = \left[\frac{\sum_{x,y=h} (\phi_{1,2|\text{LBE}} - \phi_{1,2|\text{ex}})^2}{\sum_{x,y=h} (\phi_{1,2|\text{ex}})^2} \right]^{1/2}, \quad (40)$$

$$E_{2,\text{qint}} = \left[\frac{\sum_{x,y=h} \left(D_{1,2} \frac{\partial \phi_{1,2}}{\partial y} \Big|_{\text{LBE}} - D_{1,2} \frac{\partial \phi_{1,2}}{\partial y} \Big|_{\text{ex}} \right)^2}{\sum_{x,y=h} \left(D_{1,2} \frac{\partial \phi_{1,2}}{\partial y} \Big|_{\text{ex}} \right)^2} \right]^{1/2}, \quad (41)$$

where E_2 contains the relative errors in the interior domain, $E_{2,\text{tint}}$ and $E_{2,\text{qint}}$ evaluate the relative errors of the macroscopic value ϕ and its flux at the interface, respectively, that are obtained from Eqs. (22a), (22b) and (23a), (23b). As emphasized earlier, the present conjugate interface treatment yields the same ϕ_{int} values computed from Eqs. (22a) and (22b) and the same interface flux values from Eqs. (23a) and (23b),

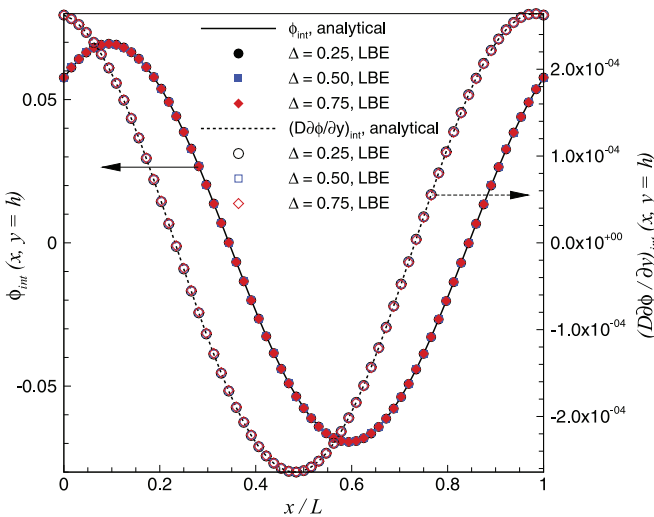


FIG. 6. (Color online) Profiles of $\phi_{\text{int}}(x, y = h)$ and $(D\partial\phi/\partial y)_{\text{int}}(x, y = h)$ at the interface ($y = h$) in the channel with the same parameters as in Fig. 5.

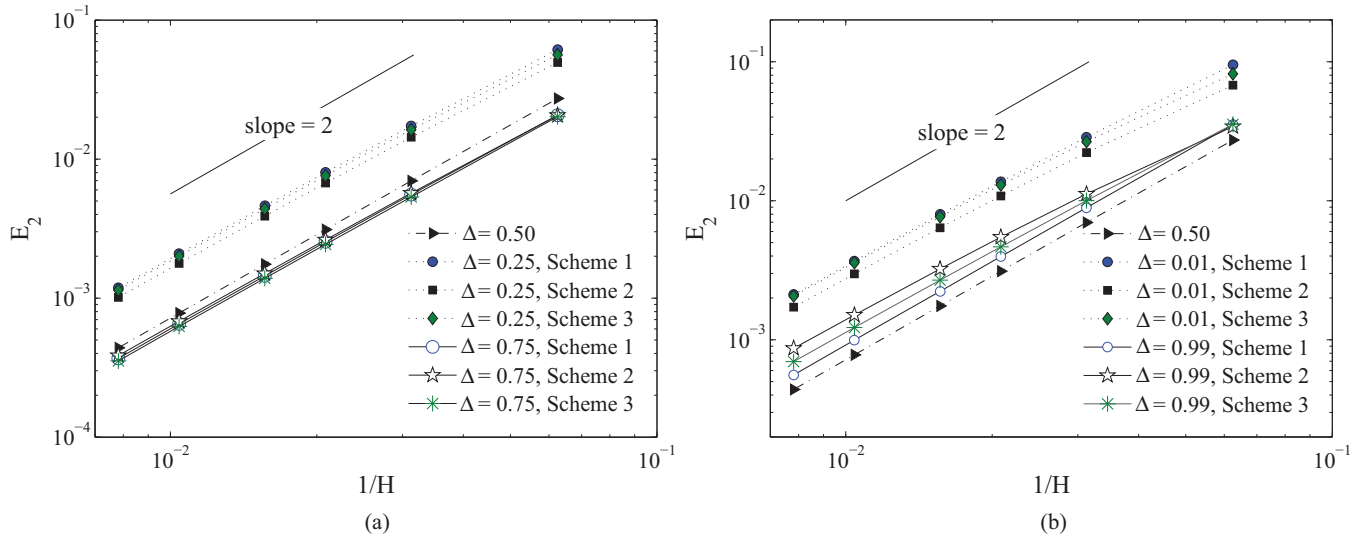


FIG. 7. (Color online) Relative L_2 norm error, E_2 , for the interior field of ϕ versus the grid resolution, $1/H$, for steady convection-diffusion in the channel using the present interface schemes with (a) $\Delta = 0.50, 0.25$, and 0.75 , and (b) $\Delta = 0.50, 0.01$, and 0.99 .

respectively, with the distribution functions in the two subdomains. For the HLD scheme used, the interface values in Eqs. (40) and (41) are computed separately from the distribution functions in the subdomains. The second-order accuracy of the Dirichlet schemes for the boundary walls has been verified in [14] and thus is not discussed here.

Figure 7 shows the results of E_2 versus the grid resolution $1/H$ at different Δ values. The relaxation coefficients are fixed at $\tau_1 = 0.55$ and $\tau_2 = 1.0$ so that the diffusivity ratio is $\kappa = (\tau_2 - 0.5)/(\tau_1 - 0.5) = 10$. The results of E_{2_tint} and E_{2_qint} are plotted in Figs. 8 and 9, respectively. The overall relative errors E_{2_qint} for the interfacial flux are higher than E_{2_tint} for the interfacial values of ϕ . Clearly, second-order convergence with respect to the spatial resolution is observed for all cases in Figs. 7–9. The second-order accuracy of the interior distributions of ϕ , the interfacial ϕ values, and its

interfacial fluxes is thus verified for straight interfaces with the present conjugate interface treatment.

To gain more insights into the effect of the link fraction Δ value on the accuracy of the conjugate interface schemes, we also show the results of E_2 , E_{2_tint} , and E_{2_qint} obtained from the modified HLD scheme [see Eqs. (28) and (29)] in Figs. 10, 11, and 12, respectively. The schemes “HLD-S1, -S2, and -S3” should be interpreted in such a way that the HLD scheme is used for the lattice nodes adjacent to the interface on both sides irrespective of the Δ value, while the actual Δ value is taken into account in the Dirichlet boundary schemes for the channel walls as well as for computing the interfacial ϕ values and the interfacial fluxes. Note that with the HLD scheme used, the interfacial values of $\phi(x, y = h)$ and $D\phi/\partial y(x, y = h)$ computed from the distribution functions in the two different domains [see Eqs. (22a), (22b)

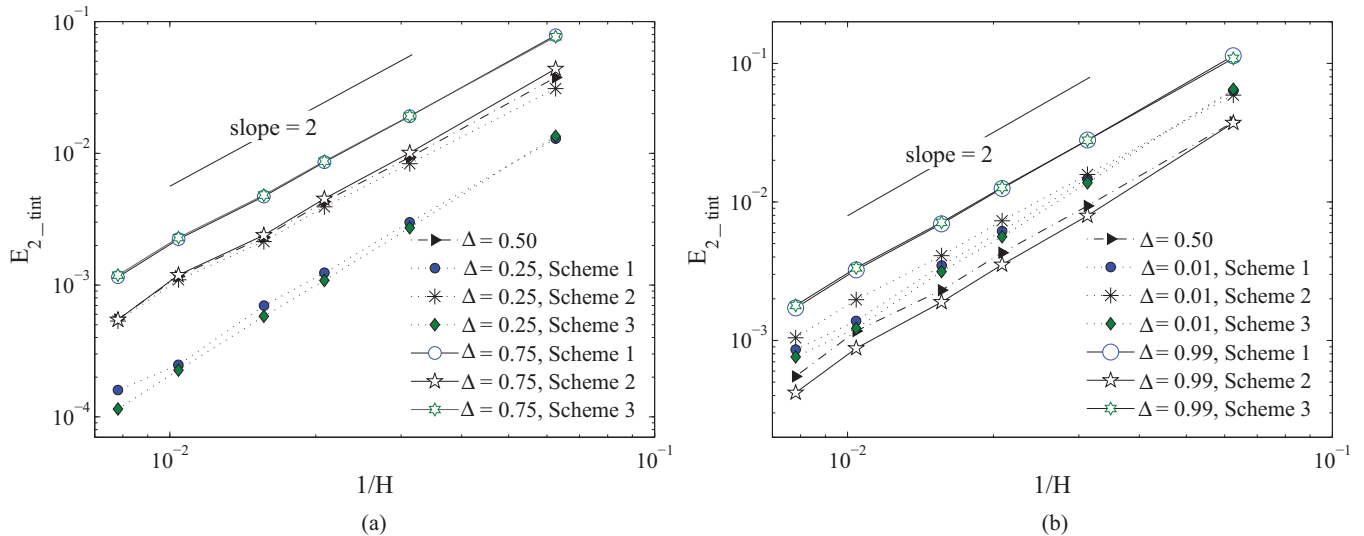


FIG. 8. (Color online) Relative L_2 norm error, E_{2_tint} , for the interfacial value of ϕ versus $1/H$ for steady convection-diffusion in the channel using the present interface schemes with (a) $\Delta = 0.50, 0.25$, and 0.75 , and (b) $\Delta = 0.50, 0.01$, and 0.99 .

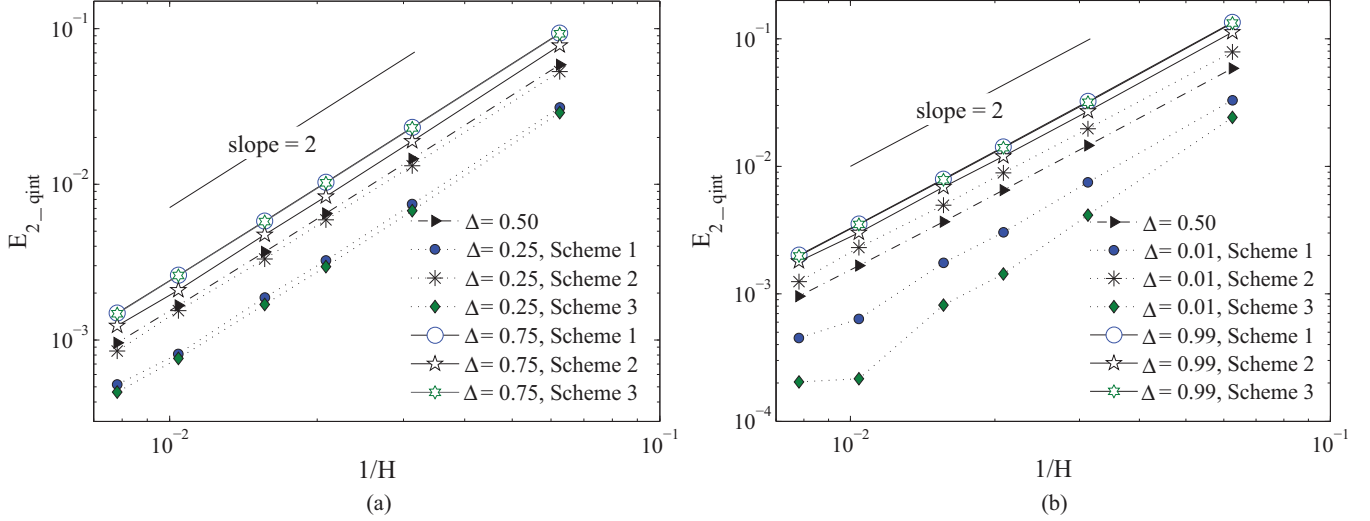


FIG. 9. (Color online) Relative L_2 norm error, $E_{2,qint}$, for the interfacial flux versus $1/H$ for steady convection-diffusion in the channel using the present interface schemes with (a) $\Delta = 0.50, 0.25$, and 0.75 , and (b) $\Delta = 0.50, 0.01$, and 0.99 .

and (23a), (23b)] are not conserved as shown in Figs. 11 and 12. As expected, only first-order convergence is obtained for each case in Figs. 10–12. This observation serves as a foundation for the error analysis in curved interface simulations when using the HLD schemes that are discussed in Secs. VB and VC.

Before moving on to curved interfaces, an unsteady problem involving the same channel flow configuration is studied next to verify the applicability and first-order temporal accuracy of the present interface treatment for time-dependent problems.

2. Unsteady convection-diffusion in the channel

For the present unsteady problem, the Dirichlet boundary conditions in Eq. (31) are replaced with

$$\phi_1(x, y = 0, t) = \phi_2(x, y = H, t) = \cos(kx + \omega t), \quad (42)$$

where $\omega = 2\pi/\Gamma$ is the frequency and Γ is the period of the imposed boundary conditions. In addition to the Péclet number, another characteristic number, the Stokes number,

$St \equiv \sqrt{\frac{H^2\omega}{2\pi D_1}} = \sqrt{\frac{H^2}{\Gamma D_1}}$, is defined for this unsteady problem following the unsteady numerical tests in [14,15,20]. The analytical solutions for $\phi_{1,2}$ in Eq. (30) subject to the Dirichlet conditions in Eq. (42) and the conjugate conditions in Eqs. (32) and (33) are

$$\phi_{ex,1}(x, y, t) = \text{Re}\{e^{i(kx+\omega t)}[\gamma_1 e^{-\lambda_1 y} + (1 - \gamma_1)e^{\lambda_1 y}]\} \quad (0 \leq y \leq h), \quad (43)$$

$$\phi_{ex,2}(x, y, t) = \text{Re}\{e^{i(kx+\omega t)}[\gamma_2 e^{-\lambda_2 y} + (1 - \gamma_2 e^{-\lambda_2 H}) \times e^{-\lambda_2(H-y)}]\} \quad (h \leq y \leq H), \quad (44)$$

where the coefficients γ_1 and γ_2 have the same expressions as in Eqs. (36) and (37), respectively, and the substitutions $\lambda_{1,2} = k \sqrt{1 + i \frac{\omega + Uk}{D_{1,2} k^2}}$ should be made in all related equations.

Initial conditions for the distribution functions are crucial in unsteady simulations. In this test, the treatment for the initial condition $g_\alpha(x, y, t = 0) = (\omega_\alpha + \frac{\delta t v_j}{\delta x \varepsilon_D} e_{\alpha j} \omega_\alpha) \phi_0 - \delta x \frac{\partial \phi_0}{\partial x_j} (M^{-1} S^{-1} M e_j \omega)_\alpha$ proposed in [13] is applied, where $\phi_0 = \phi(x, y, t = 0)$ is obtained from Eqs. (43) and (44) by setting $t = 0$. Following [14,20], the time-averaged relative errors for ϕ in the channel, the interfacial values of ϕ and its interfacial fluxes are defined in the following to assess the spatial and temporal accuracy of the present conjugate interface treatment

$$E_2 = \left\{ \frac{1}{\Gamma} \int_0^\Gamma \left[\sum_{x,y} (\phi_{LBE} - \phi_{ex})^2 / \sum_{x,y} \phi_{ex}^2 \right] dt \right\}^{1/2}, \quad (45)$$

$$E_{2,tint} = \left\{ \frac{1}{\Gamma} \int_0^\Gamma \left[\sum_{x,y=h} (\phi_{1,2|LBE} - \phi_{1,2|ex})^2 / \sum_{x,y=h} (\phi_{1,2|ex})^2 \right] dt \right\}^{1/2}, \quad (46)$$

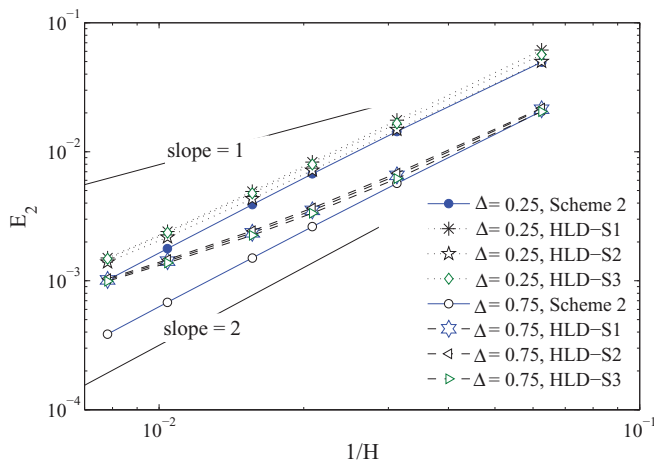


FIG. 10. (Color online) Comparison of E_2 obtained using the present interface Scheme 2 with that from the HLD scheme for steady convection-diffusion in the channel.

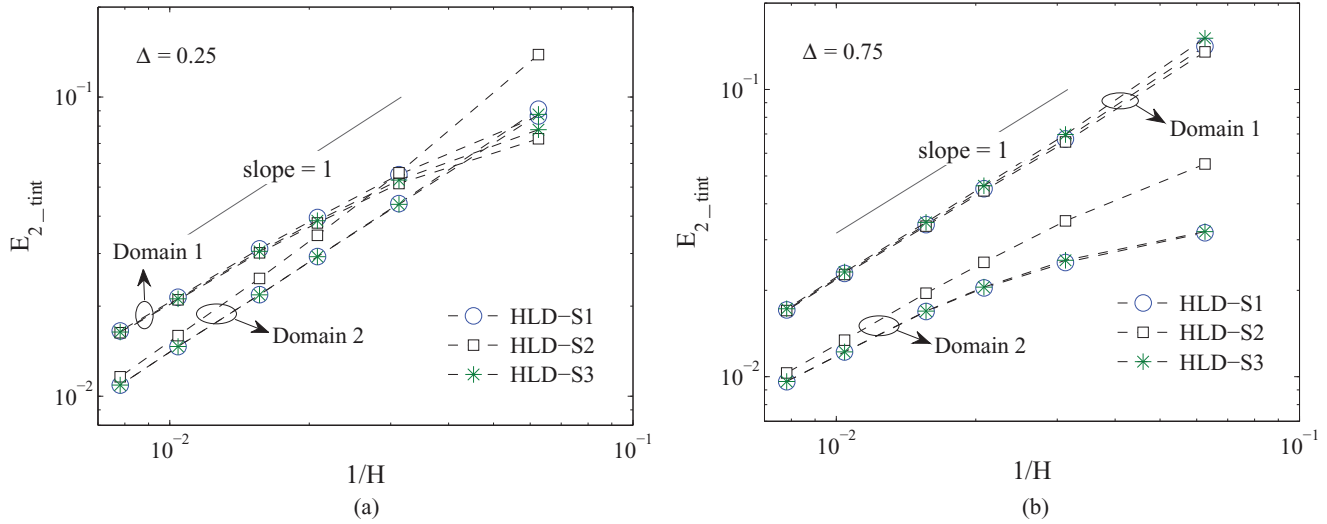


FIG. 11. (Color online) $E_{2,tint}$ versus $1/H$ obtained using the HLD scheme for steady convection-diffusion in the channel with (a) $\Delta = 0.25$ and (b) $\Delta = 0.75$.

$$E_{2,qint} = \left\{ \frac{1}{\Gamma} \int_0^\Gamma \left[\sum_{x,y=h} \left(D_{1,2} \frac{\partial \phi_{1,2}}{\partial y} \Big|_{LBE} - D_{1,2} \frac{\partial \phi_{1,2}}{\partial y} \Big|_{ex} \right)^2 / \sum_{x,y=h} \left(D_{1,2} \frac{\partial \phi_{1,2}}{\partial y} \Big|_{ex} \right)^2 \right] dt \right\}^{1/2}. \tag{47}$$

The results of E_2 , $E_{2,tint}$, and $E_{2,qint}$ defined in the above versus the grid resolution $1/H$ at $Pe = 20$ and $St = 1$ are shown in Figs. 13, 14, and 15, respectively. The diffusion coefficient ratio is again at $\kappa = 10$ ($\tau_2 = 0.55$, $\tau_1 = 1.0$) and three cases with $\sigma = (\rho c_p)_2 / (\rho c_p)_1 = 0.1, 1.0, \text{ and } 10$ are computed. Only the results from using conjugate Scheme 2 are presented in Figs. 13–15 since all three schemes give similar results as demonstrated in the steady-state test.

Second-order convergence is observed for each case in Figs. 13–15. It should be noted that the errors contain both temporal and spatial contributions. As discussed in [20], when the spatial resolution $H/\delta y$ is doubled, in order to keep the same characteristic Stokes number, $St = \sqrt{\frac{H^2}{\Gamma D_1}}$, the period of the Dirichlet boundary condition, Γ , must be quadrupled, which equivalently leads to a reduction in the dimensionless time step, $\delta t/\Gamma$, by a factor of four. Thus, although the temporal accuracy is only first order in the LBE method as verified by the asymptotic analysis in [13], the doubling in H leads to a fourfold decrease in both the spatial and the temporal errors, and thus the overall second-order convergence is obtained in Figs. 13–15. This unsteady test demonstrates that the proposed interface treatment can be effectively applied to simulate transient conjugate heat and mass transfer problems, and the second-order spatial accuracy and first-order temporal accuracy are preserved.

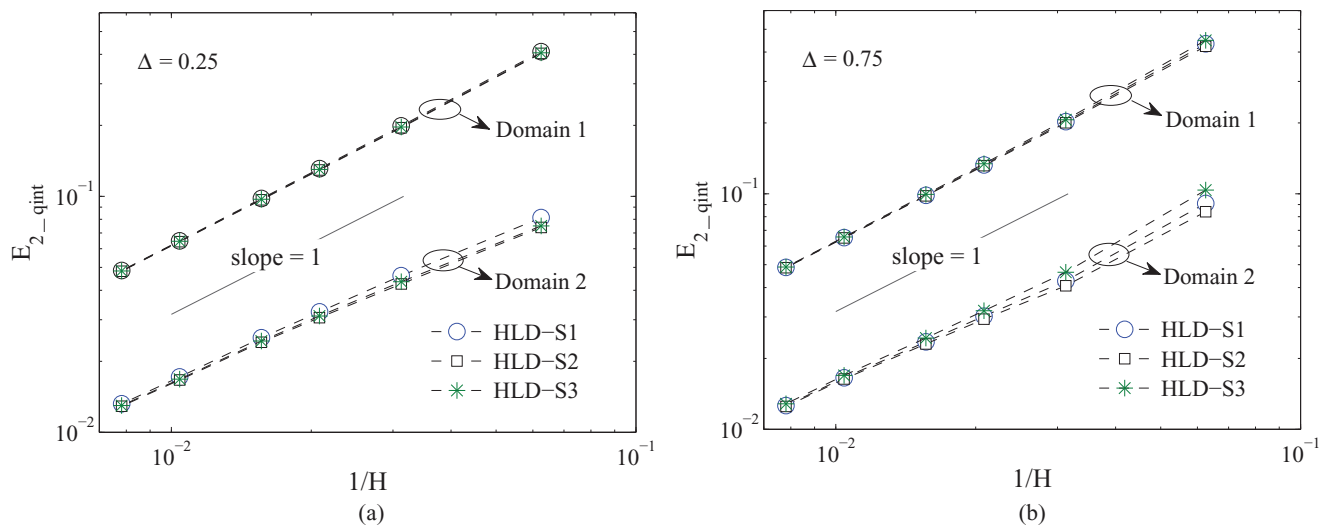


FIG. 12. (Color online) $E_{2,qint}$ versus $1/H$ obtained using the HLD scheme for steady convection-diffusion in the channel with (a) $\Delta = 0.25$ and (b) $\Delta = 0.75$.

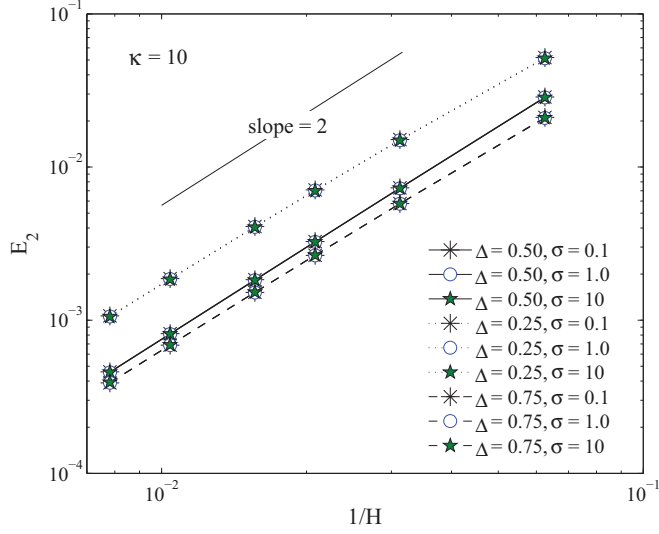


FIG. 13. (Color online) Time-averaged L_2 norm error, E_2 , versus $1/H$ for unsteady convection-diffusion in the channel using the present interface Scheme 2.

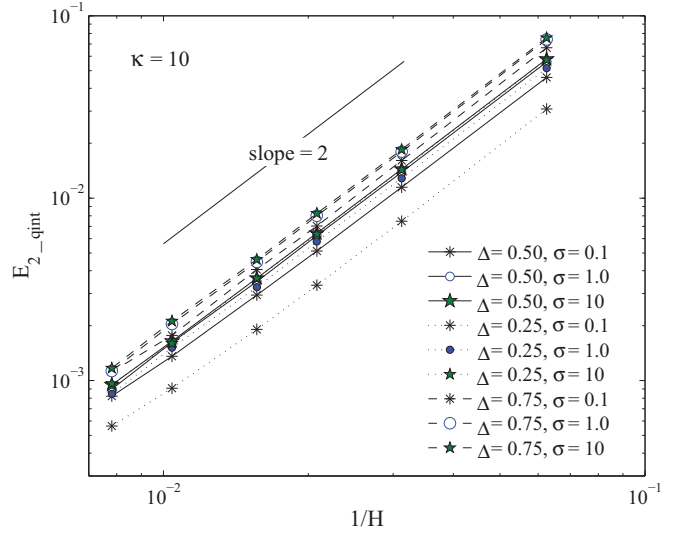


FIG. 15. (Color online) Time-averaged L_2 norm error, $E_{2,qint}$, versus $1/H$ for unsteady convection-diffusion in the channel using the present interface Scheme 2.

B. Steady heat conduction in a circular domain with two solids

The computational domain and the lattice layout are schematically depicted in Fig. 16. The curved geometry at the interface and the outer boundary is preserved by calculating the exact link fractions Δx and Δy for the lattice nodes adjacent to the interface and the outer boundary (see P_1 and P_2 in Fig. 16). After the local link fractions are calculated, the present interface treatment at $r = R_1$ and the outer boundary treatment at $r = R_2$ can be implemented.

We consider the steady-state conduction with an outer Dirichlet boundary condition

$$\phi_2(r = R_2) = f(\varphi) = \cos(n\varphi); \quad n = \text{integer}, \quad (48)$$

and the conjugate conditions at the interface

$$\phi_1 = \phi_2 \quad \text{at } r = R_1, \quad (49)$$

and

$$k_1 \frac{\partial \phi_1}{\partial r} = k_2 \frac{\partial \phi_2}{\partial r} \quad \text{at } r = R_1. \quad (50)$$

The exact solutions for the temperatures are

$$\phi_{ex,1}(r, \varphi) = a_1 r^n \cos(n\varphi) \quad (0 \leq r \leq R_1), \quad (51)$$

$$\phi_{ex,2}(r, \varphi) = (a_2 r^n + a_3 r^{-n}) \cos(n\varphi) \quad (R_1 \leq r \leq R_2), \quad (52)$$

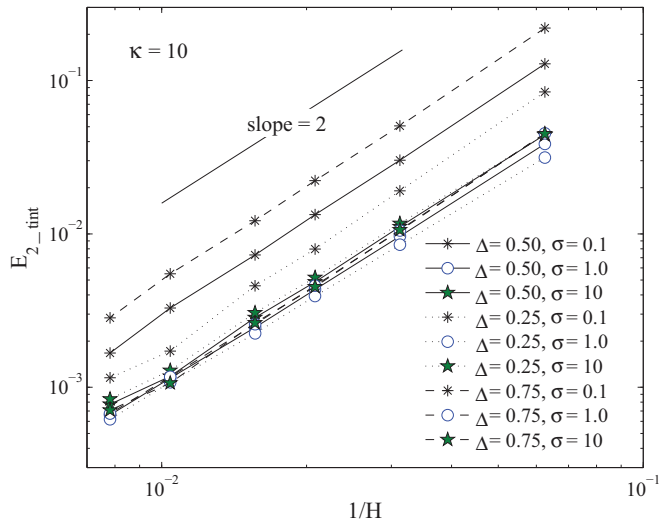


FIG. 14. (Color online) Time-averaged L_2 norm error, $E_{2,tint}$, versus $1/H$ for unsteady convection-diffusion in the channel using the present interface Scheme 2.

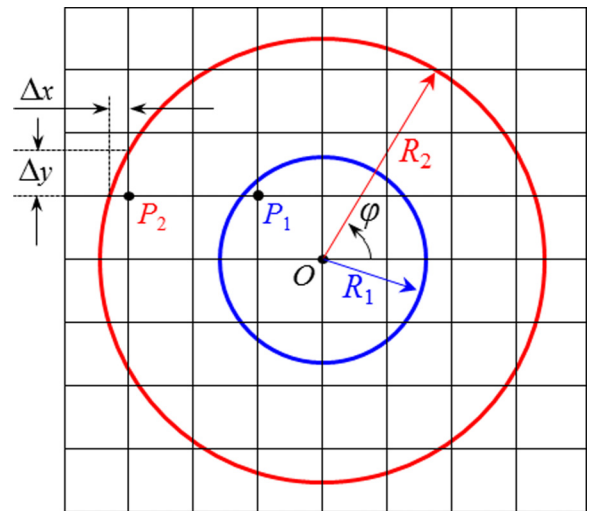


FIG. 16. (Color online) Schematic depiction of the lattice in a 2D circular domain with a curved interface and a curved outer boundary.

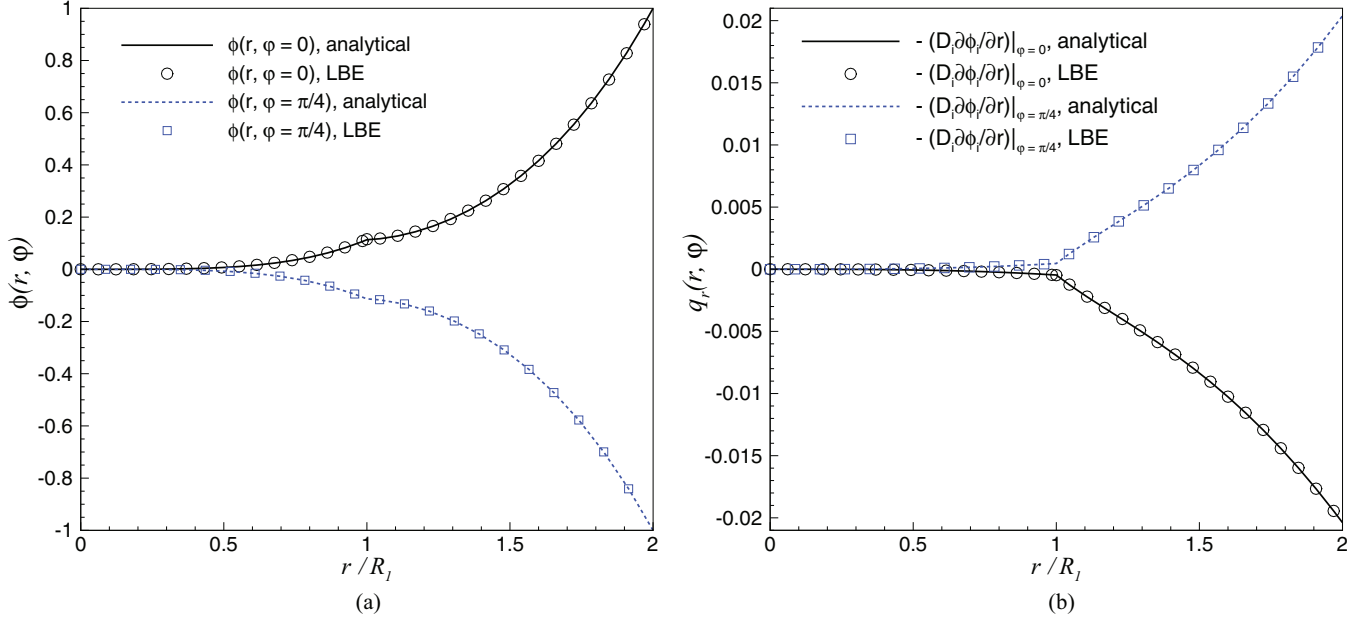


FIG. 17. (Color online) Profiles of (a) $\phi(r, \varphi)$ and (b) $q_r = -D_i \partial \phi_i / \partial r$ along the lines with constant $\phi = 0$ and $\phi = \pi/4$, respectively, in the circular domain with $R_2 = 2R_1 = 32.5\delta x$, $\kappa = 10$, $\tau_1 = 0.55$, $\tau_2 = 1.0$, and $n = 4$.

where

$$a_1 = \frac{2(k_2/k_1)R_1^{-2n}R_2^{-n}}{[(k_2/k_1) + 1]R_1^{-2n} + [(k_2/k_1) - 1]R_2^{-2n}}, \quad (53a)$$

$$a_2 = \frac{[(k_2/k_1) + 1]R_1^{-2n}R_2^{-n}}{[(k_2/k_1) + 1]R_1^{-2n} + [(k_2/k_1) - 1]R_2^{-2n}}, \quad (53b)$$

$$a_3 = \frac{[(k_2/k_1) - 1]R_2^{-n}}{[(k_2/k_1) + 1]R_1^{-2n} + [(k_2/k_1) - 1]R_2^{-2n}}. \quad (53c)$$

For present steady-state heat conduction simulations, the governing equation of CDE (1) becomes a pure diffusion equation; thus, the diffusion coefficients are set to be equal to the thermal conductivities, i.e., $D_{1,2} = k_{1,2}$, and $\sigma = (\rho c_p)_2 / (\rho c_p)_1 = 1$ can be directly used. In addition, the macroscopic velocities in the equilibrium moments $\mathbf{m}^{(eq)}$ in Eq. (3) are set to zero. For the Dirichlet condition at the outer boundary $r = R_2$, the boundary schemes in [14] (also given in Appendix B) are used. For the conjugate condition at $r = R_1$, the presently proposed coupled interface treatment in Eqs. (19a) and (19b) with the coefficients determined in Table I for the particular Schemes 1, 2, and 3 are implemented and their simulation results are compared with that from the HLD scheme in Eq. (29).

First, the profiles of ϕ and its flux $q_r = -D_i \partial \phi_i / \partial r$ along the lines starting at the origin O with $\phi = 0$ and $\pi/4$ are examined in Figs. 17(a) and Figs. 17(b), respectively. The simulated results agree very well with analytical solutions [$q_{r,LBE} = (\Phi_{nx,LBE}^2 + \Phi_{ny,LBE}^2)^{1/2}$ is used in Fig. 17(b)]. The interfacial values of ϕ_{int} and flux q_{int} versus ϕ are shown in Figs. 18(a) and 18(b), respectively. Note that the interfacial fluxes $q_{int} = -D_i \partial \phi_i / \partial x$ and $-D_i \partial \phi_i / \partial y$ directly evaluated from the present interface treatment are in the Cartesian lattice velocity directions. For the curved interface it is also verified that the numerical values of ϕ_{int} and q_{int} evaluated from the distribution functions in the two subdomains are exactly the

same. It can be observed in Figs. 18(a) and 18(b) that the numerical errors for the interfacial flux q_{int} are relatively larger than that for ϕ_{int} . The numerical accuracy for those interfacial quantities as well as the interior distribution of ϕ with curved interfaces is further investigated next.

Figures 19, 20, and 21 show the L_2 norm errors E_2 , $E_{2,tint}$, and $E_{2,qint}$ defined in Eqs. (39), (40), and (41), respectively, versus the grid resolution $1/R_1$ at $R_2/R_1 = 2$ and $n = 4$ in Eq. (48). It should be noted that in the present case E_2 is evaluated in the circular domain $0 \leq r \leq R_2$, $E_{2,tint}$ and $E_{2,qint}$ are evaluated at the interface $r = R_1$, and both $\partial \phi / \partial y$ and $\partial \phi / \partial x$ are included in the evaluation of $E_{2,qint}$. For comparison purposes, the simulation results from using the previous conjugate interface schemes in [9–11,16], which are denoted as the HLD scheme in Eq. (29), are also included in Figs. 19–21. Again, “Domain 1” and “Domain 2” in Figs. 20 and 21 represent the interfacial temperature and flux computations from the distribution functions at the lattice nodes in Domain 1 ($0 \leq r \leq R_1$) and Domain 2 ($R_1 \leq r \leq R_2$), respectively. It is emphasized that even for the cases with the HLD scheme used for the interface, the interfacial temperature and fluxes are also obtained from the evaluation techniques in Eqs. (22) and (23), which include the local Δ values. The results in Figs. 19–21 indicate that the computed interior temperature field and interfacial temperature values are second-order accurate and the interfacial flux (temperature gradient) is first-order accurate when the present interface Schemes 1, 2, and 3 are used. The quadratic convergence of the interior temperature field and the linear convergence of the interfacial flux are consistent with the results reported in [14,15] for the interior temperature distributions and the boundary fluxes, respectively, in Dirichlet problems with curved boundaries. The degradation of the convergence orders from quadratic to linear for the boundary and interfacial fluxes is attributed to the irregularly distributed link fraction Δ values. In contrast, only first-order accurate interior and interfacial

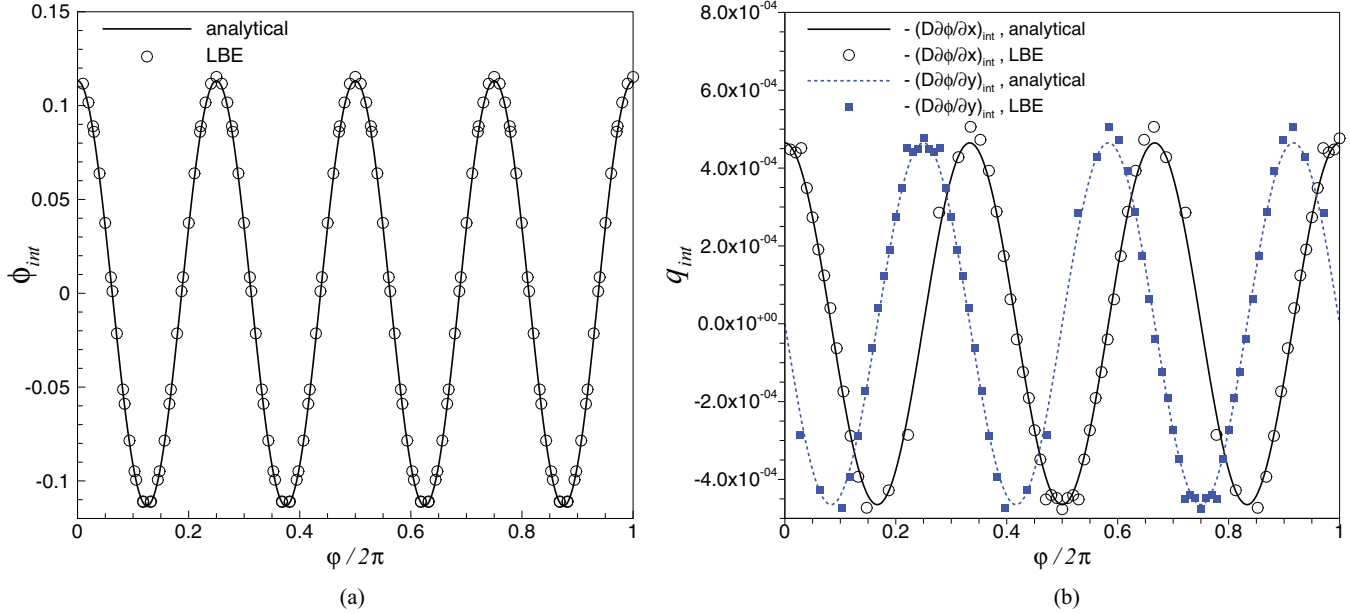


FIG. 18. (Color online) Profiles of (a) $\phi_{int}(r, \varphi)$ and (b) $q_{int} = -(D\partial\phi/\partial x)_{int}$ or $-(D\partial\phi/\partial y)_{int}$ at the interface in the circular domain with the same parameters as in Fig. 17.

temperatures are obtained in Figs. 19 and 20, respectively, when the HLD scheme is used for the interface condition and for which a zeroth-order accurate interfacial flux is noticed in Fig. 21. In general, the numerically computed interfacial fluxes have higher relative errors than that for the interfacial values of ϕ for each case tested when one compares the results in Figs. 20 and 21. The present conjugate interface treatment that takes into account the local link fractions at a curved interface is clearly able to improve the order of accuracy of the LBE results by one degree for each of the three quantities, including the interior temperature field, the interfacial temperatures, and the interfacial fluxes compared with the simple HLD scheme that has been widely used in the literature.

C. Unsteady mass transfer from a spherical droplet in an external creeping flow

Conjugate mass transfer from a spherical droplet of radius R immersed in an ambient fluid of large extent is considered in this test. With the focus on the conjugate mass transfer on the droplet boundary (the interface between the droplet and the outside fluid), the fluid flow far away from the droplet, \mathbf{u}_∞ , is assumed to be a simple extensional flow represented by

$$\mathbf{u}_\infty = \underline{\underline{E}}\mathbf{x}, \quad \underline{\underline{E}} = \begin{pmatrix} -1/2 & 0 & 0 \\ 0 & -1/2 & 0 \\ 0 & 0 & -1/2 \end{pmatrix} E, \quad (54)$$

where \mathbf{x} is the spatial position vector, $\underline{\underline{E}}$ is the rate-of-strain tensor, and E is the strength of the extension rate. When scaled by ER , the analytical solutions for the dimensionless velocity

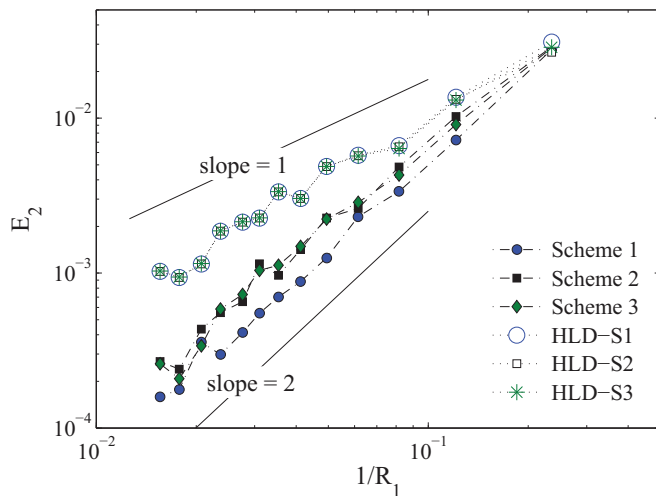


FIG. 19. (Color online) Comparison of E_2 obtained using the present interface schemes with that from the HLD scheme for steady heat conduction in the circular domain with a curved interface.

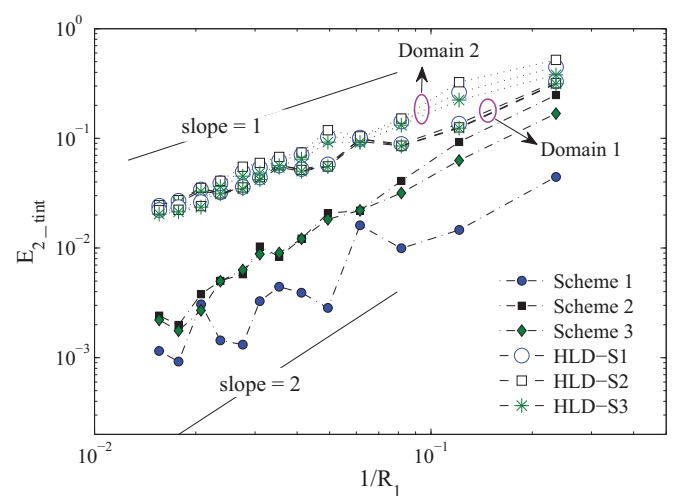


FIG. 20. (Color online) Comparison of $E_{2,int}$ obtained using the present interface schemes with that from the HLD scheme for steady heat conduction in the circular domain with a curved interface.

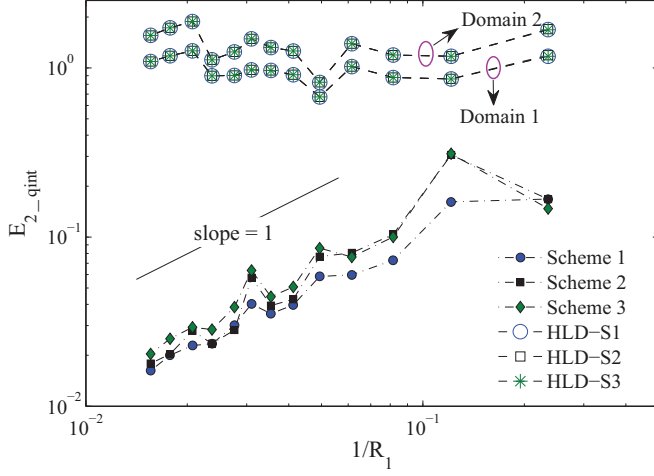


FIG. 21. (Color online) Comparison of $E_{2,qint}$ obtained using the present interface schemes with that from the HLD scheme for steady heat conduction in the circular domain with a curved interface.

field are [7,8]

$$u_{1r} = \left(1 - \frac{3}{2}\sin^2\theta\right) \left[r^* - \frac{5\lambda + 2}{2(\lambda + 1)(r^*)^2} + \frac{3\lambda}{2(\lambda + 1)(r^*)^4} \right],$$

$$u_{1\theta} = -\frac{3}{2}\sin\theta\cos\theta \left[r^* - \frac{\lambda}{(\lambda + 1)(r^*)^4} \right], \quad (r^* \geq 1) \quad (55)$$

$$u_{1\phi} = 0,$$

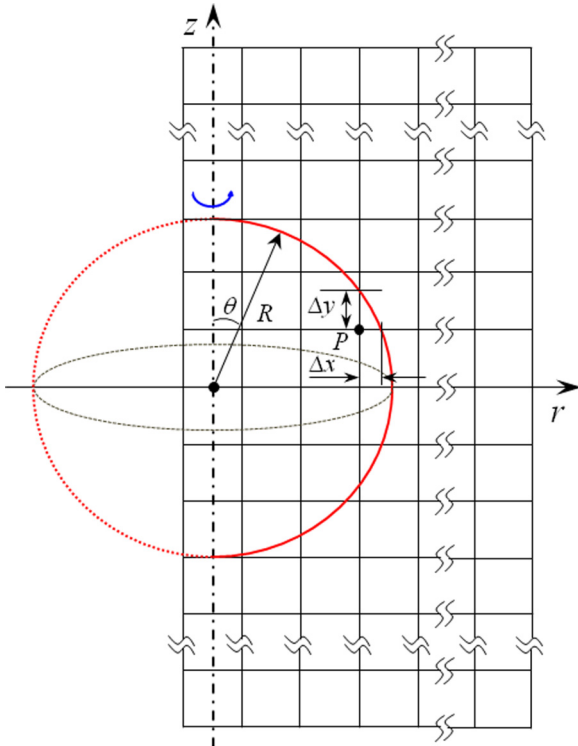


FIG. 22. (Color online) Schematic depiction of the computational domain and the square lattice layout for conjugate mass transfer across the interface of a spherical droplet immersed in an extensional creeping flow.

and

$$u_{2r} = \left(1 - \frac{3}{2}\sin^2\theta\right) \left[-\frac{3r^*}{2(\lambda + 1)} + \frac{3(r^*)^3}{2(\lambda + 1)} \right],$$

$$u_{2\theta} = -\frac{3}{2}\sin\theta\cos\theta \left[-\frac{3r^*}{2(\lambda + 1)} + \frac{5(r^*)^3}{2(\lambda + 1)} \right], \quad (0 \leq r^* \leq 1)$$

$$u_{2\phi} = 0, \quad (56)$$

where $r^* = r/R$, θ is the polar angle and ϕ is the azimuthal angle in the spherical coordinate system, and λ is the viscosity ratio of the fluid inside the droplet ($0 \leq r^* \leq 1$) to that outside the droplet ($r^* \geq 1$). Note that only the uniaxial extensional flow is considered in this work and $\lambda = 1$ is used in all simulations. Assuming that the initial mass concentrations are uniform at ϕ_{01} and ϕ_{02} for the exterior fluid and the droplet, respectively, and the mass transfer process does not affect the flow field or the shape of the droplet at any time, both the flow field [see Eqs. (55) and (56)] and the concentration field are axisymmetric with no variations in the ϕ direction.

The initial condition, the far-field boundary conditions and the conjugate interface conditions are written as

$$\phi_1 = \phi_{01} (r > R) \text{ and } \phi_2 = \phi_{02} (0 \leq r \leq R) \text{ at } t = 0, \quad (57)$$

$$\phi = \phi_{01} (r \gg R), \quad (58)$$

$$\phi_1 = \phi_2 \text{ at } r = R, \quad (59)$$

and

$$D_1 \frac{\partial \phi_1}{\partial r} = D_2 \frac{\partial \phi_2}{\partial r} \text{ at } r = R. \quad (60)$$

The characteristic Péclet numbers are $Pe_{1,2} = ER^2/D_{1,2}$, and the overall Sherwood number, Sh , for the mass transfer at the interface is defined as [7,8]

$$Sh = \frac{\bar{h}R}{D_2} = \frac{QR}{4\pi R^2 D_2 \Delta\bar{\phi}_2}, \quad (61)$$

where $\bar{h} = -D_2 \frac{\partial \phi_2}{\partial r} |_{r=R} / \Delta\bar{\phi}_2$ is the averaged mass transfer coefficient at the interface, Q is the total mass transfer rate

$$Q = 2\pi R^2 \int_0^\pi \left(-D_2 \frac{\partial \phi_2}{\partial r} |_{r=R} \right) \sin\theta d\theta, \quad (62)$$

and $\Delta\bar{\phi}_2$ denotes the difference between the interior bulk concentration and the far-field concentration

$$\Delta\bar{\phi}_2 = \bar{\phi}_2 - \phi_{01} = \frac{\int_0^R \int_0^\pi (\phi_2 - \phi_{01}) r^2 \sin\theta d\theta dr}{\int_0^R \int_0^\pi r^2 \sin\theta d\theta dr}$$

$$= \frac{3}{2R^3} \int_0^R \int_0^\pi (\phi_2 - \phi_{01}) r^2 \sin\theta d\theta dr. \quad (63)$$

This problem can be simulated with either the standard D3Q7 model by preserving the geometry at the curved interface or with the axisymmetric D2Q5 model proposed in [20]. The present work focuses on the conjugate interface treatment; thus, the 2D axisymmetric model is used for most of the simulations to demonstrate the accuracy. For the purpose of demonstrating the applicability of the conjugate interface

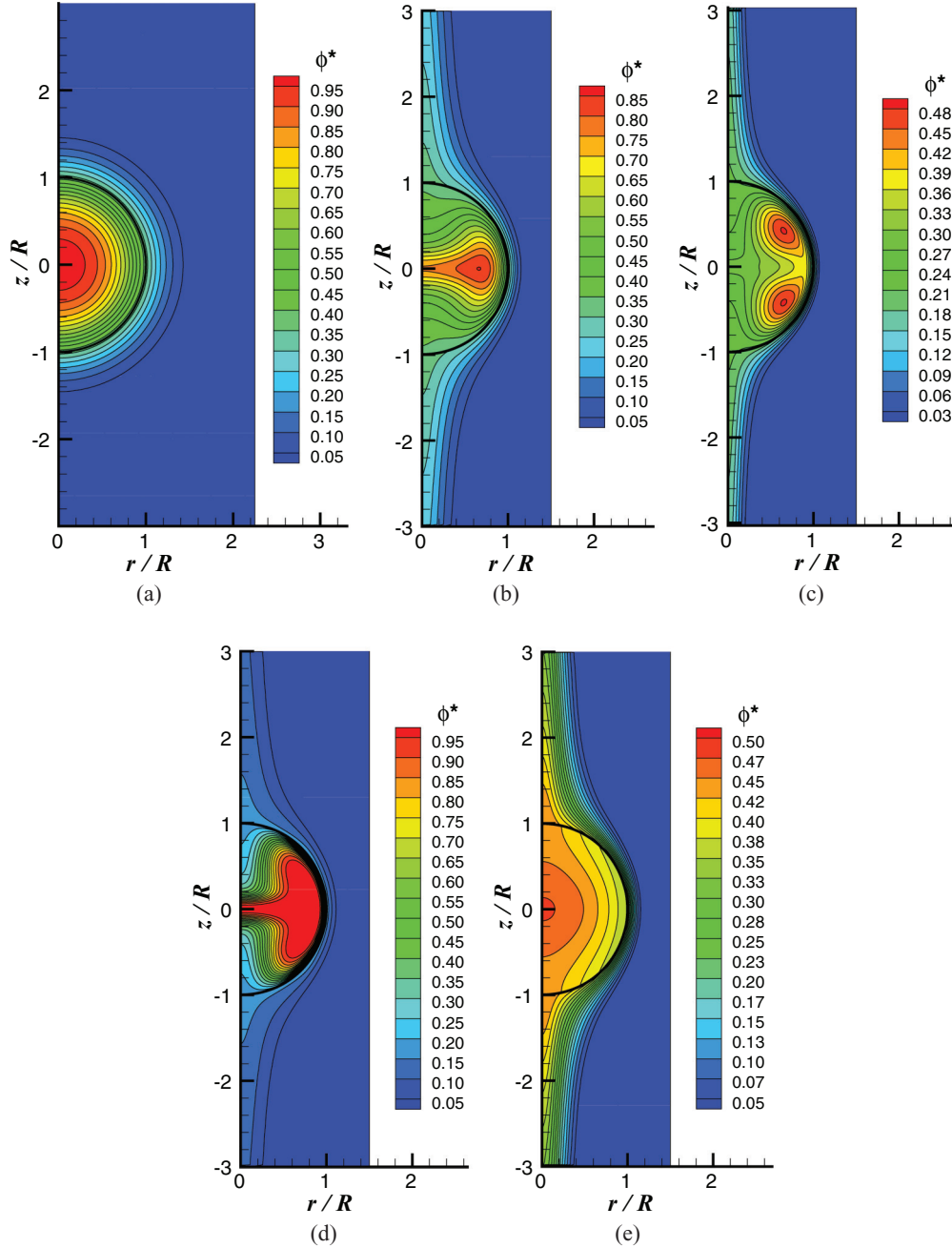


FIG. 23. (Color online) Dimensionless concentration contours for mass transfer from the droplet in the extensional creeping flow at $Fo_1 = 5 \times 10^{-2}$ and (a) $Pe_1 = 1$, $D_2/D_1 = 1$; (b) $Pe_1 = 100$, $D_2/D_1 = 1$; (c) $Pe_1 = 500$, $D_2/D_1 = 1$; (d) $Pe_1 = 100$, $D_2/D_1 = 0.1$; and (e) $Pe_1 = 100$, $D_2/D_1 = 10$.

treatment in a true 3D simulation, the 3D LBE model is used to compute the mass transfer problem for $Pe_1 \leq 100$. In the 2D LBE model, the axisymmetric CDE for mass concentration in the spherical coordinate system is represented in the radial-axial cylindrical coordinate system [20]. The computational domain and the square lattice layout are schematically illustrated in Fig. 22, where the curved geometry at the interface $r = R$ is preserved by calculating the lattice link fractions in both directions, similar to that in Fig. 16. For the conjugate interface conditions, the coupled interface treatment in Eqs. (19a) and (19b) with the coefficients from

Scheme 2 in Table I is implemented. The far-field boundaries are considered as straight boundaries.

To compute the total mass transfer rate Q in Eq. (62) on the curved interface, the heat and mass transfer evaluation technique proposed in [15] is employed rather than using any finite-difference schemes based on the simulated concentration field. Thus, the mass transfer rate is obtained from

$$Q = 2\pi R \sum_{x_w} \sum_{\bar{\alpha}} \Phi_{n\bar{\alpha}} \delta x \sin \theta, \quad (64)$$

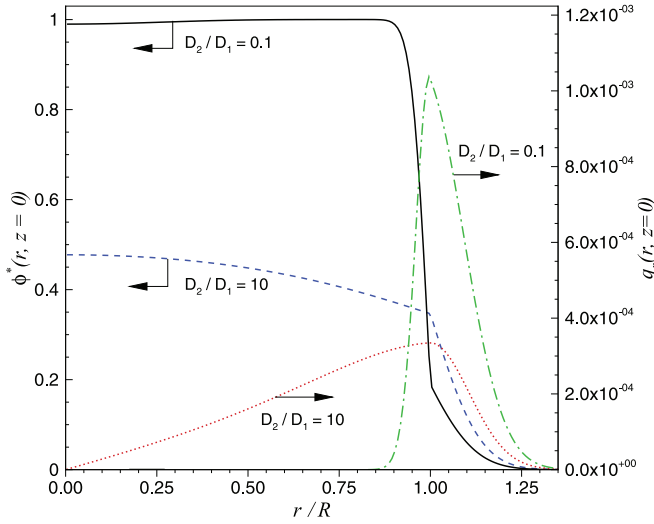


FIG. 24. (Color online) Profiles of $\phi^*(r, z)$ and $q_r = -D_i \partial \phi_i^* / \partial r$ along the horizontal line at $z = 0$ for Cases (d) and (e) in Fig. 23.

where $\Phi_{n\bar{\alpha}}$ represents the mass flux in the lattice velocity direction $\mathbf{e}_{\bar{\alpha}}$ at an interface node \mathbf{x}_w , δx is the unit lattice spacing, and θ is the local polar angle at \mathbf{x}_w . The integral in Eq. (63) is approximated from the summation of the integrands evaluated at all the interior lattice nodes within the droplet. As pointed out in [8] and also observed in present simulations, the Sherwood number defined in Eq. (61) approaches an asymptotic value Sh_∞ for each case after a long period of time.

Figure 23 shows some typical transient distributions of the dimensionless concentration $\phi_{1,2}^* = \frac{\phi_{1,2} - \phi_{01}}{\phi_{02} - \phi_{01}}$ at different Pe_1 and D_2/D_1 values at $Fo_1 = 5 \times 10^{-2}$, where Fo_1 is the Fourier number defined as $Fo_1 = D_1 t / R^2$. Since the time step in the presently used LBE model is $\delta t = 1$, the relaxation coefficient $\tau = \frac{1}{2} + \frac{\delta t}{\varepsilon_D (\delta x)^2} D$ [see Eq. (4)] is chosen in such a way that $t = Fo_1 R^2 / D_1 = N \delta t$, with N being an integer. The diffusivity ratio is maintained at $D_2/D_1 = 1$ in Figs. 23(a)–23(c) at $Pe_1 = 1, 100$, and 500 , respectively, while in Figs. 23(d) and 23(e) the results from $D_2/D_1 = 0.1$ and 10 , respectively, are compared at the same $Pe_1 = 100$. The concentration contours in Fig. 23(a) are almost parallel to the curved interface, representing the dominating diffusion effect over the weak convection at $Pe_1 = 1$. As Pe_1 increases, the effect of convection becomes more significant and thin boundary layers near the droplet surface are clearly seen on each side of the interface in Figs. 23(b) and 23(c). The center of the contours with maximum concentration has shifted from the droplet center in Fig. 23(a) to the region near the surface along the horizontal r coordinate [see

Fig. 23(b)]. It further splits into two symmetric regions with local maximum concentrations as observed in Fig. 23(c). The present concentration distributions agree well qualitatively with the results shown in [8]. The different thicknesses of the boundary layers inside and outside the droplet near the interface in Figs. 23(d) and 23(e) correspond to their diffusivity difference. Recalling the flux continuity $D_1 \frac{\partial \phi_1}{\partial r} = D_2 \frac{\partial \phi_2}{\partial r}$ in Eq. (60), the concentration gradient $\partial \phi_2 / \partial r$ inside the droplet ($r/R < 1$) is much higher than $\partial \phi_1 / \partial r$ outside the droplet since $D_2/D_1 = 0.1$ in Fig. 23(d), and the opposite case with $D_2/D_1 = 10$ is noticed in Fig. 23(e). This can also be explained by the plotted profiles of ϕ_i^* and its flux $q_r = -D_i \partial \phi_i^* / \partial r$ along the horizontal line at $z = 0$ as shown in Fig. 24.

To quantitatively verify the present LBE simulations, the asymptotic values of the surface-averaged Sherwood number, Sh_∞ , are computed and compared with some of the results reported in [8]. The convergence of Sh_∞ is checked with respect to the grid resolution, the locations of the far-field boundaries and the time duration. A typical grid resolution $R = 128$ with $N_r = 3R$, $N_z = 6R$ (N_r and N_z denote the grid numbers in the r and z directions, respectively) is used, and the number of evolutionary time steps is on the order of 10^5 . For some cases with high Péclet number, higher grid resolution is used to ensure computational stability and accuracy. For all cases, the relaxation coefficients τ_1 and τ_2 are retained in the range of $0.51 \leq \tau \leq 2.0$. Table III compares the numerical values of Sh_∞ obtained from D2Q5 with those from Ref. [8] for $1 \leq Pe_1 \leq 2000$ at a fixed diffusivity ratio $D_2/D_1 = 10$. The third row includes the results from the D3Q7 model and the present conjugate interface treatment. The relaxation coefficients are fixed at $\tau_1 = 0.525$ and $\tau_2 = 0.75$. For the computations using the 2D axisymmetric model (denoted as 2D axisym.), the radius and grid numbers are $(R, N_r, N_z) = (25, 251, 513)$ for $Pe_1 = 1$, $(64, 201, 641)$ for $Pe_1 = 5$ and 10 , $(128, 261, 641)$ for $Pe_1 = 50, 100$, and 200 , and $(256, 361, 1541)$ for $Pe_1 = 500, 800, 1000$, and 2000 , respectively. For the 3D results in Table III, $(R, N_x, N_y, N_z) = (25.5, 151, 151, 151)$ for $Pe_1 = 1$, and $(25.5, 101, 181, 101)$ for $Pe_1 = 5, 10, 50$, and 100 are used. Three-dimensional computation for very high Péclet number $Pe_1 > 100$ is not conducted due to the large computational time and memory needed to resolve the very thin boundary layer near the interface. For the low Péclet number case, $Pe_1 = 1$, the mass diffusion is significant over the entire domain and a larger domain is needed. Thus, for the axisymmetric model, $R_\infty/R = 10$ is used. The 3D result has a larger error than that from the 2D axisymmetric model because the computational domain is smaller with $y_\infty/R = z_\infty/R = 2.94$ in the 3D computation. To demonstrate this more clearly, two more cases are computed for $Pe_1 = 1$ using the 2D axisymmetric model with $R_\infty/R = 6/\sqrt{\pi}$ and $R_\infty/R = 3$.

TABLE III. Comparison between present LBE computations with published results for Sh_∞ versus Pe_1 with $D_2/D_1 = 10$.

Pe_1	Average Sherwood number Sh_∞									
	1	5	10	50	100	200	500	800	1000	2000
Ref. [8]	0.305	1.046	1.584	3.578	4.872	6.527	9.713	12.10	13.61	18.49
Present (2D axisym.)	0.309	1.059	1.587	3.613	4.920	6.587	9.702	12.15	13.48	18.53
Present (3D)	0.358	1.045	1.521	3.352	4.378					

TABLE IV. Comparison between the results for Sh_∞ versus D_2/D_1 at $Pe_1 = 100$.

D_2/D_1	Average Sherwood number Sh_∞									
	0.1	0.2	1	2	5	10	20	30	50	100
Ref. [8]	1.311	2.010	3.401	3.811	4.472	4.872	5.136	5.246	5.289	5.366
Present	1.202	1.953	3.433	3.849	4.512	4.920	5.140	5.194	5.234	5.383

The resulting values are $Sh_\infty = 0.359$ and 0.383 , respectively. The first case has the same effective computational domain as that in the 3D case in Table III for $Pe_1 = 1$ [the volume of computational domain $V = \pi(6R/\sqrt{\pi})^2(6R) = (6R)^3$] and the result of $Sh_\infty = 0.359$ from the axisymmetric 2D model is in excellent agreement with $Sh_\infty = 0.358$ from the 3D model. In the second case, a further decrease in R_∞/R from 3.39 to 3 results in an increase of Sh_∞ from 0.359 to 0.383, thus clearly demonstrating the effect of the domain size on the mass transport when the computational domain is relatively small and Pe_1 is low. For large Péclet number cases, the 3D results have larger errors than the 2D results because of the lower grid resolution used.

Tables IV and V show the dependence of Sh_∞ on D_2/D_1 at constant Péclet numbers $Pe_1 = 100$ and 1000 , respectively. It should be noted that some extreme cases with high Péclet number up to $Pe_1 = 10^5$ were also computed in [8], where grid stretching was applied; while in this work simulations for very high Péclet number cases are not conducted since (i) very high resolution is required to capture the thin boundary layers with uniformly spaced square lattice used in the present LBE model, and (ii) with the assumption of creeping flow (low Reynolds flow, $Re \ll 1$) used for the velocity field in [8] as well as in the present work, high Péclet number flows imply that the Prandtl number Pr for the fluids should be extremely large ($Pr = Pe/Re$), which is impractical for most fluids. Thus, only the simulation results at moderate Pe_1 , Pe_2 , and D_2/D_1 values ($Pe_1/Pe_2 = D_2/D_1$) are presented in Tables III–V. Overall, the present LBE results for the Sherwood number are in good agreement with those reported in [8], demonstrating that the present conjugate interface treatment in the LBE method is capable of simulating mass transfer problems with curved interfaces.

VI. CONCLUSIONS

A general second-order accurate interface treatment for conjugate heat and mass transfer simulations using the LBE method is proposed based on our previous second-order accurate Dirichlet and Neumann boundary condition treatments. The continuity of the macroscopic variable (temperature in

heat transfer or concentration in mass transfer) and its flux at the interface is intrinsically satisfied on the level of the microscopic distribution functions in the present treatment. Thus, the iteration on the interface as usually used in traditional CFD methods based on the macroscopic temperature or concentration field during each time step is not required. The interfacial temperature or concentration and their fluxes are conveniently obtained with no extrapolation needed. Three particular interface schemes for the general interface treatment are provided, and they can be greatly simplified for special cases such as straight interfaces and zero-tangential-gradient interfaces.

The second-order accuracy of the interior temperature (concentration) field, the interfacial temperature (concentration) and the interfacial fluxes using the proposed interface schemes is verified with numerical tests for steady and unsteady convection-diffusion in a channel with a straight interface. When curved interfaces are encountered, the numerical test for heat conduction within a circular domain of two solids demonstrates that the interface treatment is able to give second-order accurate interior and interfacial temperatures and first-order accurate interfacial heat flux. An improvement of order of accuracy by one degree is gained for all of these three quantities compared with the ‘‘HLD’’ interface scheme that has been widely used in the literature. Another numerical test for unsteady mass transfer from a spherical droplet in an extensional creeping flow demonstrates that the present interface treatment is robust and can be used to simulate convection-diffusion problems with conjugate interface transport and strong boundary layers. The application of the present conjugate interface treatment to heat and mass transfer coupled with hydrodynamic fluid flows is an area for future study.

ACKNOWLEDGMENTS

This paper was prepared with the support of the U.S. Department of Energy, ARPA-E, under Award No. DE-AR0000184.

APPENDIX A: D3Q7 AND D2Q5 LBE MODELS FOR THE CONVECTION-DIFFUSION EQUATION

The transformation matrix M for the D3Q7 model is [13]

$$M = \begin{bmatrix} 1 & 1 & 1 & 1 & 1 & 1 & 1 \\ 0 & 1 & -1 & 0 & 0 & 0 & 0 \\ 0 & 0 & 0 & 1 & -1 & 0 & 0 \\ 0 & 0 & 0 & 0 & 0 & 1 & -1 \\ 6 & -1 & -1 & -1 & -1 & -1 & -1 \\ 0 & 2 & 2 & -1 & -1 & -1 & -1 \\ 0 & 0 & 0 & 1 & 1 & -1 & -1 \end{bmatrix}, \quad (A1)$$

TABLE V. Comparison between the results for Sh_∞ versus D_2/D_1 at $Pe_1 = 1000$.

D_2/D_1	Average Sherwood number Sh_∞						
	2	5	10	20	30	50	100
Ref. [8]	10.74	12.78	13.61	14.24	14.60	15.08	15.52
Present	10.52	12.70	13.55	14.20	14.59	15.00	15.43

and the relaxation matrix S is [13]

$$S^{-1} = \begin{bmatrix} \tau_0 & 0 & 0 & 0 & 0 & 0 & 0 \\ 0 & \tau_{xx} & \tau_{xy} & \tau_{xz} & 0 & 0 & 0 \\ 0 & \tau_{xy} & \tau_{yy} & \tau_{yz} & 0 & 0 & 0 \\ 0 & \tau_{xz} & \tau_{yz} & \tau_{zz} & 0 & 0 & 0 \\ 0 & 0 & 0 & 0 & \tau_4 & 0 & 0 \\ 0 & 0 & 0 & 0 & 0 & \tau_5 & 0 \\ 0 & 0 & 0 & 0 & 0 & 0 & \tau_6 \end{bmatrix}. \quad (\text{A2})$$

As pointed out in [13], the off-diagonal components in the relaxation matrix can take nonzero values to account for anisotropic diffusion. The relaxation coefficients are related to the diffusion coefficient matrix as

$$\tau_{ij} = \frac{1}{2} \delta_{ij} + \frac{\delta t}{\varepsilon_D (\delta x)^2} D_{ij}, \quad (\text{4a})$$

in order to recover the solution of the CDE to the leading order.

The weight coefficients are [13]

$$\omega_\alpha = \begin{cases} 1/4, & (\alpha = 0), \\ 1/8, & (\alpha = 1, 2, 3, 4, 5, 6), \end{cases} \quad (\text{A3})$$

and the constant $\varepsilon_D = 1/4$ for the 3D model. As given in [14], the constant a in $\mathbf{m}^{(\text{eq})}$ is related to the coefficients ω_α by $a = (7\omega_0 - 1) = 3/4$.

For the D2Q5 model, the details are [13,14]

$$M = \begin{bmatrix} 1 & 1 & 1 & 1 & 1 \\ 0 & 1 & -1 & 0 & 0 \\ 0 & 0 & 0 & 1 & -1 \\ 4 & -1 & -1 & -1 & -1 \\ 0 & 1 & 1 & -1 & -1 \end{bmatrix}, \quad (\text{A4})$$

$$S^{-1} = \begin{bmatrix} \tau_0 & 0 & 0 & 0 & 0 \\ 0 & \tau_{xx} & \tau_{xy} & 0 & 0 \\ 0 & \tau_{xy} & \tau_{yy} & 0 & 0 \\ 0 & 0 & 0 & \tau_3 & 0 \\ 0 & 0 & 0 & 0 & \tau_4 \end{bmatrix}, \quad (\text{A5})$$

$$\omega_\alpha = \begin{cases} 1/3 & (\alpha = 0), \\ 1/6 & (\alpha = 1, 2, 3, 4), \end{cases} \quad (\text{A6})$$

with $\varepsilon_D = 1/3$ and $a = (5\omega_0 - 1) = 2/3$.

APPENDIX B: PARTICULAR BOUNDARY SCHEMES FOR THE DIRICHLET CONDITION

Dirichlet boundary Scheme 1,

$$g_{\bar{\alpha}}(\mathbf{x}_f, t + \delta t) = \begin{cases} (-2\Delta) \hat{g}_\alpha(\mathbf{x}_f, t) + (2\Delta - 1) \hat{g}_\alpha(\mathbf{x}_{ff}, t) + \varepsilon_D \Phi_d & (0 \leq \Delta \leq 0.5), \\ (-\frac{1}{2\Delta}) \hat{g}_\alpha(\mathbf{x}_f, t) + (1 - \frac{1}{2\Delta}) \hat{g}_\alpha(\mathbf{x}_f, t) + (\frac{1}{2\Delta}) \varepsilon_D \Phi_d & (\Delta > 0.5), \end{cases} \quad (\text{B1})$$

Dirichlet boundary Scheme 2,

$$g_{\bar{\alpha}}(\mathbf{x}_f, t + \delta t) = 2(\Delta - 1) \hat{g}_\alpha(\mathbf{x}_f, t) - \left[\frac{(2\Delta - 1)^2}{2\Delta + 1} \right] \hat{g}_\alpha(\mathbf{x}_{ff}, t) + 2 \left(\frac{2\Delta - 1}{2\Delta + 1} \right) \hat{g}_{\bar{\alpha}}(\mathbf{x}_f, t) + \left(\frac{3 - 2\Delta}{2\Delta + 1} \right) \varepsilon_D \Phi_d, \quad (\text{B2})$$

and Dirichlet boundary Scheme 3,

$$g_{\bar{\alpha}}(\mathbf{x}_f, t + \delta t) = -\hat{g}_\alpha(\mathbf{x}_f, t) + \left(\frac{2\Delta - 1}{2\Delta + 1} \right) \hat{g}_\alpha(\mathbf{x}_{ff}, t) + \left(\frac{2\Delta - 1}{2\Delta + 1} \right) \hat{g}_{\bar{\alpha}}(\mathbf{x}_f, t) + \left(\frac{2}{2\Delta + 1} \right) \varepsilon_D \Phi_d. \quad (\text{B3})$$

-
- [1] B. Roe, R. Jaiman, A. Haselbacher, and P. H. Geubelle, *Int. J. Numer. Methods Fluids* **57**, 329 (2008).
- [2] A. Dorfman and Z. Renner, *Math. Prob. Eng.* **2009**, 927350 (2009).
- [3] W. D. Henshaw and K. K. Chand, *J. Comput. Phys.* **228**, 3708 (2009).
- [4] J. Lindström and J. Nordström, *J. Comput. Phys.* **229**, 5440 (2010).
- [5] M. P. Errera and S. Chemin, *J. Comput. Phys.* **245**, 431 (2013).
- [6] L. Li, R. Mei, J. F. Klausner, and D. W. Hahn, *ASME J. Heat Transfer* **134**, 011301 (2012).
- [7] J. Zhang, C. Yang, and Z. S. Mao, *AICHE J.* **58**, 3214 (2012).
- [8] J. Zhang, C. Yang, and Z. S. Mao, *Chem. Eng. Sci.* **79**, 29 (2012).
- [9] J. Wang, M. Wang, and Z. Li, *Int. J. Therm. Sci.* **46**, 228, (2007).
- [10] M. Wang, J. Wang, N. Pan, and S. Chen, *Phys. Rev. E* **75**, 036702 (2007).
- [11] M. Wang and N. Pan, *Int. J. Heat Mass Transfer* **51**, 1325 (2008).
- [12] L. Chen, Q. Kang, Y. L. He, and W. Q. Tao, *Int. J. Hydrogen Energy* **37**, 13943 (2012).
- [13] H. Yoshida and M. Nagaoka, *J. Comput. Phys.* **229**, 7774 (2010).
- [14] L. Li, R. Mei, and J. F. Klausner, *J. Comput. Phys.* **237**, 366 (2013).
- [15] L. Li, R. Mei, and J. F. Klausner, *ASME J. Heat Transfer* **136**, 012403 (2014).
- [16] A. Tarokh, A. A. Mohamad, and L. Jiang, *Numer. Heat Transfer, Part A: Appl.* **63**, 159 (2013).
- [17] F. Meng, M. Wang, and Z. Li, *Int. J. Heat Fluid Flow* **29**, 1203 (2008).
- [18] G. Imani, M. Maerefat, and K. Hooman, *Numer. Heat Transfer, Part A: Appl.* **62**, 798 (2012).
- [19] M. Seddiq, M. Maerefat, and M. Mirzaei, *Int. J. Therm. Sci.* **75**, 28 (2014).
- [20] L. Li, R. Mei, and J. F. Klausner, *Int. J. Heat Mass Transfer* **67**, 338 (2013).
- [21] R. Mei, L.-S. Luo, and W. Shyy, *J. Comput. Phys.* **155**, 307 (1999).